TECHNISCHE UNIVERSITÄT WIEN

Acoustic Optimisation of an Electric Ducted Fan Unit through Absorber Design and Placement

Master's Thesis

Jakob Schmidt

TECHNISCHE UNIVERSITÄT WIEN

DIPLOMARBEIT

Acoustic Optimisation of an Electric Ducted Fan Unit through Absorber Design and Placement

ausgeführt zum Zwecke der Erlangung
des akademischen Grades eines Diplom-Ingenieurs
unter der Leitung von

Dipl.-Ing. Dr.techn. Stefan Schoder
Univ.-Prof. Dipl.-Ing. Dr.techn. Manfred Kaltenbacher
Institut für Mechanik und Mechatronik, E325-A3

im Auftrag von und in Kooperation mit
VOLARE GmbH

eingereicht an der Technischen Universität Wien
Fakultät für Maschinenwesen und Betriebswissenschaften
von

Jakob Schmidt
[redacted]

Wien, am 19. Oktober 2020

Contents

Nomenclature

Acronyms

AC	alternating current
BL	boundary layer
BPF	blade passing frequency
BTS	blade tip speed
CFRP	carbon fibre reinforced polymer
DC	direct current
DoF	degree of freedom
ECM	electronically commutated motor
EDF	electric ducted fan
ESM	enveloping surface method
ESC	electronic speed controller
eVTOL	electric vertical take-off and landing
GDP	gross domestic product
ICAO	International Civil Aviation Organization
LE	leading edge
MPA	microperforated panel absorber
MPP	microperforated panel
MSA	microsliced absorber
MPT	multiple pure tones
OGV	outlet guide vane
OSPL	overall sound pressure level
PTS	propulsion test stand
PU	propulsion unit
SPL	sound pressure level
TE	trailing edge

Latin letters

a	hub radius

a	perforation radius
a_{mn}	amplitude parameter of (m, n)-mode
$a_{m\mu}$	amplitude parameter of (m, μ)-mode
a_n	amplitude parameter of n-mode
A_{Rotor}	fan rotor area
A	equivalent sound absorption area
b	tip radius
B	rotor blades
c	local speed of sound
c_0	speed of sound
c_{0i}	speed of sound of fan i
c_∞	speed of sound reference value
C	characteristic fan constant
d	length of layer
d_i	length of layer i
d_{Rotor}	fan rotor diameter
$d_{\mathrm{Rotor}i}$	fan rotor diameter of fan i
d_x	axial separation of rotor and stator
d_0	fan rotor diameter reference value
D	perforation distance
e	source-dependent exponent
f	frequency
f_{c}	center frequency
f_{BPF}	blade passing frequency
$f_{\mathrm{BPF}n}$	n^{th} blade passing frequency harmonic
f_{LF}	frequency of electromagnetic local forces
$f_{\mathrm{LF}n}$	n^{th} harmonic frequency of electromagnetic local forces
f_{max}	maximum frequency without time-dependent aliasing
f_{max1}	maximum frequency without spatial aliasing
f_{max2}	maximum frequency for rotating sources
f_{min}	minimum frequency to distinguish separate sources
f_{s}	sampling time
F_{T}	aerodynamic thrust force
He	Helmholtz number
J_m	m-mode's first kind Bessel function
J_0	first kind Bessel function of zero order
J_1	first kind Bessel function of first order
k	whole number of spinning pattern
k	characteristic wave number
$k\prime$	characteristic number for microperforation impedance
k_i	characteristic wave number of layer i
$k_{x\mu}$	exponential decay rate

$k_{m\mu}$	characteristic Bessel function number
$k_{m\mu}^{'(\sigma)}$	characteristic Bessel function number
K_1	external noise correction factor
K_2	room reflection correction factor
L	characteristic length
L_p	sound pressure level
$\overline{L_p}$	time- and space-averaged sound pressure level
$L_{pi(\mathrm{B})}$	time-averaged sound pressure level of external noise at microphone i
$\overline{L_{p(\mathrm{B})}}$	time-averaged sound pressure level of external noise
$L'_{pi(\mathrm{ST})}$	time-averaged sound pressure level of measuring object at microphone i
$\overline{L_{p(\mathrm{ST})'}}$	time-averaged sound pressure level of measuring object
$L_{p,\mathrm{norm}}$	relative sound pressure level
$\overline{L_{PA}}_{\mathrm{norm}}$	relative A-weighted sound pressure level
L_W	sound power level
$\overline{L_W}$	time- and space-averaged sound power level
L_{Wi}	sound power level of fan i
$L_{W\mathrm{s}}$	sound power level constant
m	lobe number of spinning pattern
m	Mach number exponent
m_{a}	acoustic mass per unit area
M_m^*	m-mode's Mach number
M_m^*	m-mode's critical Mach number
M_{tip}	blade tip Mach number
n	harmonic order
n_{T}	dimension of sound propagation
N	rotational speed
N	number of array microphones
N_{M}	number of microphones
p	pressure distribution
p	electric motor pole number
$\hat{p}$	acoustic pressure constant
p_{a}	acoustic pressure
p_μ	pressure distribution of μ-mode
$p_{m\mu}$	in-duct pressure distribution of (m, μ)-mode
$P_{m\mu}$	far-field pressure distribution of (m, μ)-mode
P	aerodynamically generated sound power
P_{abs}	absorbed acoustic energy
P_{inc}	incident acoustic energy
P_{T}	mechanic power
Q	characteristic Bessel number
r	radial cylindrical coordinate
r_{m}	acoustic resistance

r_{sl}	sparrow limit
R	radial spherical coordinate
R	reflection coefficient
S	enveloping measuring surface
S_0	enveloping measuring reference surface
St	Strouhal number
t	time coordinate
t	facesheet thickness
t_{a}	porous absorbent thickness
t_{m}	measuring time
T_n	reverberation time for a n dB decay
u	characteristic flow velocity
$\overline{u}$	flow mean velocity
u_{tip}	blade tip speed
$u_{\mathrm{tip}i}$	blade tip speed of fan i
u_0	blade tip speed reference value
v_{a}	acoustic particle velocity
V	stator vanes
V	measuring room's volume
$\dot{V}_0$	mean volume flow
x	spatial coordinate
y	spatial coordinate
z_{c}	characteristic impedance
$z_{\mathrm{c}i}$	characteristic impedance of layer i
z_{s}	surface impedance
$z_{\mathrm{s}i}$	surface impedance of layer i

Greek letters

α	sweep angle
β	lean angle
ϵ	tip speed exponent
ϵ	fraction of open area
η	dynamic viscosity
θ	angular cylindrical coordinate
θ	angle of reflected wave
θ_{a}	array aperture half angle
λ	acoustic wavelength
μ	number of Bessel function's zeros
ν	kinematic viscosity
ρ	flow medium's local density

ρ_0	flow medium's density
ρ_{0i}	flow medium's density of fan i
ρ_∞	flow medium's density reference value
ϱ_x	microphone array radius
ϱ_y	rotating source radius
σ	hub-tip ratio
φ	angle of transmitted wave
φ_m	phase parameter of m-mode
φ_{mn}	phase parameter of (mn)-mode
φ_n	phase parameter of n-mode
ψ	angular spherical coordinate
ψ	angle of incident wave
ω	angular frequency
ω	angular velocity
ω_m	angular velocity of m-mode

Abstract

Novel electric aircraft concepts are being developed by multiple aircraft manufacturers to exhaust the capabilities of modern electromobility. Their respective electric propulsion systems not only obtain different turbomachinery properties but, also exhibit different acoustical behaviour than conventional combustion turbines. The Austrian start-up *VOLARE GmbH* develops an electrically powered aircraft that can take-off and land vertically and commissioned the acoustic evaluation and optimisation of one electric propulsion unit. Thus, the present thesis' motivation was not only to examine a subscale electric ducted fan (EDF) unit regarding its acoustic characteristics across its laid-out operating range, but also to find and evaluate a noise-abating modification in the form of absorber linings.

Acoustic measurements were performed on the subsonic ducted fan, which was provided by the company *VOLARE GmbH*, in the form of total sound power and microphone array measurements to gain insight into the dominant acoustic emissions and their respective prevailing source mechanisms. Measurements at discrete operating points were conducted, as well as transient measurements, across the total operating range to provide complete information on the EDF's acoustic behaviour. The rotor-self noise and the rotor-stator interaction were identified as main tonal sound sources for the measuring object, along with the highest broadband noise sources also being located on the rotor.

Additionally, far-field measurements of the unit's electric powertrain without load were conducted, which showed significant noise emissions also coming from the periodic electromagnetic forces. Furthermore, unexpected dependencies on the rotational speed were detected in the powertrain's noise spectrum, which also contribute to the EDF's perceived acoustics.

After processing the gained insights from the first measuring campaign, a secondary noise reduction measure was applied by designing and placing perforate absorber linings to the observed fan unit's duct. Afterwards, the far-field emissions were measured once again for the modified fan unit, and compared to measurement results of the unmodified fan unit. An improvement in the fan unit's acoustic characteristics was determined through a continuously lower A-weighted overall sound pressure level of 2-4 dB across the total operating range. Moreover, a closer examination of the modified EDF's frequency spectrum across the defined operating range confirmed the frequency dependence of the designed absorbers.

Kurzfassung

Neuartige elektrische Flugzeugkonzepte werden derzeit von mehreren Flugzeugherstellern erarbeitet, um die Möglichkeiten der heutigen Elektromobilität auszuschöpfen. Die dafür entworfenen elektrischen Triebwerkssysteme haben nicht nur unterschiedliche Antriebscharakteristiken als herkömmliche Verbrennungsturbinen, sondern weisen auch unterschiedliche akustische Eigenschaften auf. Das österreichische Start-Up *VOLARE GmbH* entwickelt ein elektrisch angetriebenes, senkrecht startendes und landendes Flugzeug und beauftragte die akustische Evaluierung und Optimierung einer elektrischen Triebwerkseinheit. Die Motivation der vorliegenden Arbeit war es daher, nicht nur eine skalierte elektrische Triebwerkseinheit hinsichtlich ihrer akustischen Eigenschaften über den ausgelegten Betriebsbereich hinweg zu untersuchen, sondern auch eine lärmmindernde Modifikation in Form von Absorberauskleidungen zu finden und zu bewerten.

Akustische Messungen wurden am elektrischen Triebwerk in Form von Gesamtschallleistungs- und Mikrofonarraymessungen durchgeführt, um Erkenntnisse über die dominierenden Schallemissionen und die jeweils vorherrschenden Quellmechanismen zu gewinnen. Messungen wurden sowohl an diskreten Betriebspunkten, als auch transient über den gesamten Betriebsbereich vorgenommen, um vollständige Daten über das akustische Verhalten des Triebwerks zu erhalten. Als tonale Hauptschallquelle des Messobjekts wurden der Eigenschall des Rotors sowie die Rotor-Stator Interaktion identifiziert, wobei auch die höchsten breitbandigen Schallpegel auf den Rotor als Schallquelle zurückgeführt werden konnten.

Weiters wurden Messungen der elektronischen Komponenten des Antriebsstrangs ohne Last durchgeführt, welche signifikante tonale und schmalbandige Schallquellen auch in diesen Komponenten offenbarten. Außerdem wurden unerwartete Drehzahl-Abhängigkeiten des Lärmspektrums der elektronischen Komponenten festgestellt, die ebenfalls die Akustik des Triebwerkes beeinflussen.

Durch die Verarbeitung der gewonnenen Erkenntnisse aus der ersten Messkampagne wurde eine sekundäre Lärmminderungsmaßnahme durch die Auslegung und Platzierung perforierter Absorberauskleidungen am Kanal des untersuchten Triebwerks durchgeführt. Anschließend wurden die Fernfeldemissionen für das modifizierte Triebwerk nochmals gemessen und mit den Messergebnissen des unmodifizierten Triebwerkes verglichen. Eine Verbesserung der akustischen Eigenschaften des Triebwerkes wurde durch den kontinuierlich

niedrigeren A-bewerteten Gesamtschalldruckpegel über den gesamten Betriebsbereich festgestellt. Darüber hinaus bestätigten genauere Untersuchungen der akustischen Spektren des modifizierten Triebwerkes die erwartete Frequenzabhängigkeit der Absorberauskleidungen.

Chapter 1

Introduction

With general aviation starting to become affordable for a significant portion of the population in the 20th century, this sector has been expanding into one of the world's biggest industries with an economic impact on 3.6 % of global gross domestic product (GDP) in 2018 [1]. However, the aviation industry was still expected to expand further from 4.3 billion airline passengers in 2018 to about 10 billion by 2040 [1, 2].

As air travel has expanded, its impact on the environment has been examined on numerous occasions. Concerns about noise emissions had to be dealt with ultimately when the jet engine was introduced to general aviation aircraft in 1951 [3, 4]. Complaints from airport neighbours, flight personnel and airport staff arose due to the mental and physical consequences of constant noise exposure, which since have been permanently subject to health research [5]. The International Civil Aviation Organization (ICAO) started to create regulations on aircraft noise in 1968 and published the first edition of Annex 16 in 1971, to be applied to new aircraft designs [4]. The regulations contain precise limitations on noise levels at specific points during take-off and landing, in detail for different aircraft types [4, 6, 7].

With aircraft numbers increasing and regulations on noise emissions getting more and more stringent, manufacturers of novel aircraft, in particular, need to consider noise abatement strategies at an early stage of the design process. Additionally, social acceptance is of growing importance for new products to survive on the free market, which forces any kind of unwanted emissions to be decreased to an acceptable level. *VOLARE GmbH*, an Austrian start-up, develops an electrically powered aircraft that can take-off and land vertically (eVTOL) to provide a novel solution for individual air transport [8]. As the main acoustic sources of the mentioned eVTOL are its propulsion units (PU), a closer examination of one separate PU allows to gather conclusions of the whole vehicle noise [9, 10].

Therefore, the focus of the present diploma thesis is to evaluate one individual PU acoustically and apply secondary noise reduction measures to achieve genuinely lower noise levels. Based on the above-mentioned problem statement, two research questions are required, which are treated in the following:

- **Question 1:** What are the sound sources and the emitted sound characteristics concerning frequency spectrum and sound pressure levels of the considered propulsion unit at its operating point?
- **Question 2:** What frequency spectrum and sound pressure levels of the considered propulsion unit's flow field at the operating point can be achieved by design and placement of microperforated absorber linings?

To answer the research questions, there is a detailed discussion about the state-of-the-art in ducted fan acoustics presented in Chap. 2. Noise source mechanisms in ducted fans are treated and scientific insights are presented on how to influence the source intensities in a positive way by varying design parameters. Mathematical models of sound propagation and radiation are shown, as well as their underlying theoretical background. Additionally, scaling laws for the simplified comparison of acoustic properties between different fan model sizes are presented.

Apart from source reduction measures, secondary noise abatement measures can be taken to influence a ducted fan's acoustic characteristics. So-called absorber linings can be designed to dissipate sound energy and reduce the sound power level emitted in certain frequency bands. A literature study on these sound absorption mechanisms and the state-of-the-art in absorber design is conducted in Chap. 3 with the main focus on microperforated panel absorbers (MPA).

Chap. 4 treats the methodology used to perform the microphone array and enveloping surface method measurements. The measurement setup, as well as the postprocessing methods, are presented in this chapter. Further, Chap. 4 contains the measurement results of the PU in its unmodified state and the observed characteristics are discussed for the far-field measurements, as well as for the microphone array measurements.

Finally, the absorber design and placement in the PU are presented in Chap. 5, followed by the effects measured due to the modifications on the PU's acoustic far-field emissions. Moreover, the electric powertrain was measured solely without load after the absorber linings were applied to the PU. The respective measurement results are presented and discussed at the end of Chap. 5.

Chapter 2

Ducted fan acoustics

Ducted fan acoustics has been subject to scientific research since the first use of jet engines for aircraft propulsion systems in the early 20th century [3, 11]. Issues targeted were and still are not only the detection of the acoustic sources and the reduction of noise source mechanisms, but also to actively suppress noise pollution by the implementation of sound absorbers, which requires a detailed description of ducted fans' acoustic behaviour [12].

In this Chapter, an overview of ducted axial fan systems' acoustic properties is presented with underlying theoretical as well as experimental data from former research papers. The systems treated herein will, therefore, be ducted fan systems in general and electric ducted fan (EDF) systems, rather than jet engine systems as the examination of combustion processes is not part of this thesis.

A distinction between subsonic and supersonic fan systems can be made depending on the rotor's blade tip speed (BTS). Due to the subsonic nature of the object of study considered in Chap. 4, supersonic effects will not be examined primarily during the present thesis. Moreover, the following literature study will focus on the acoustic behaviour of single-stage fan systems with a general number of B rotor blades and V stator vanes.

A fully configured EDF system can be broken down into three component groups:

- **Stationary aerodynamic components** such as stator, inlet lip, duct, exhaust cone and exhaust end pipe;
- **Rotating aerodynamic components** such as rotor and spinner; and
- **Electric powertrains** consisting of a motor controller, electric motor and cable connections

General ducted fan systems are composed of stationary and rotating aerodynamic components only. In the present thesis, the motor controller will be considered as a component of the EDF system as it has a noticeable contribution to the system's acoustic behaviour. For further clarification of the above mentioned EDF components, an EDF system's schematic representation is depicted in Fig. 2.1. The EDF system's working principle is to transform

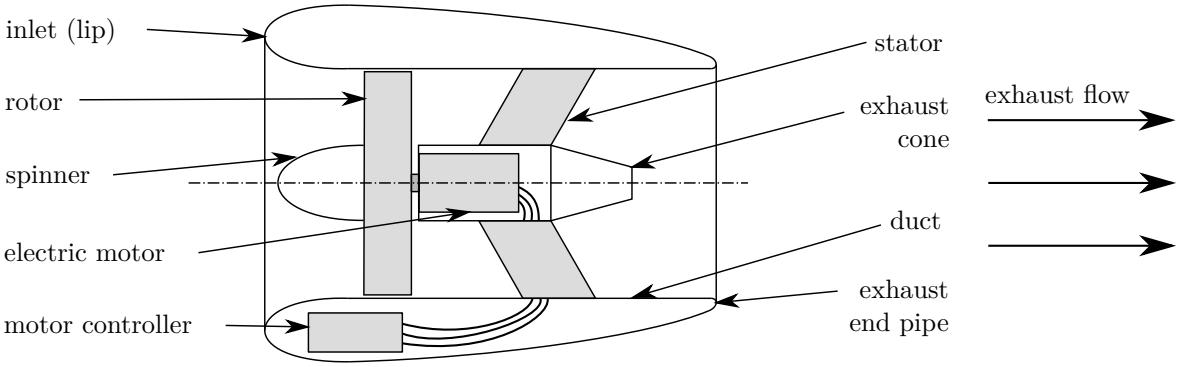

Fig. 2.1. Visualisation of components in an operational EDF system.

electrical power into aerodynamic thrust by operating an axial-flow fan with the torque produced by an electric motor. Therefore, the motor controller converts the power[1] coming from an external power source into feeding power for the electric motor.

To further delimit EDF systems from combustion turbine-powered turbofan, turbojet, and turboprop engines, which are commonly used in commercial and military aviation, Tab. 2.1 summarizes their main operational properties [11, 12].

Tab. 2.1. Working principles of different aircraft propulsion systems

	EDF	turbofan	turbojet	turboprop
energy source	elec. energy	fossil fuel	fossil fuel	fossil fuel
propulsive technology	elec. motor	turbine	turbine	turbine
engine bypass air	yes	yes	no	yes
bypass air shrouding	duct	duct	-	no
thrust by bypass air	100 %	30–70 %	0 %	100 %
thrust by turbine air	-	30–70 %	100 %	0 %

2.1 Acoustic sources

The main acoustic sources of operating ducted axial-flow fans have their origin in the developed flow field. Their causes are space- and time-dependent pressure fluctuations inside the flow field induced by rotating and stationary aerodynamic components with particular attention to rotor and stator. Other acoustic phenomena with lower magnitudes are acoustic pressure fluctuations established by vortex shedding, transient aerodynamic loading caused by turbulence, blade vibration and other flow-induced causes [13].

To provide a clear structure, the different acoustic sources are divided into four major categories which are formed by the rotor, the interaction of the rotor flow field with the stator vanes, the flow wake and the electric powertrain.

[1] Most motor controllers designed for use in vehicles operate with direct current (DC) as common mobile power supplies (e.g. lithium-ion (Li-ion) batteries) are not able to provide alternating current (AC).

2.1.1 Rotor

Rotor blades are usually modelled as twisted airfoil profiles, which are spaced evenly apart from each other in a circular manner. In order to discuss the acoustic pressure emitted by the rotor alone, its interaction with the stator vanes is omitted during the following presentation.

When a ducted fan is operated, the rotor is turned with constant angular velocity $\omega = 2\pi N$ around its rotational axis, which develops identical pressure fields around each blade that are rigidly attached to the rotor. Subsequently, the pressure must depend on the angular and time coordinates in the form $p(r, \theta, t) = p(r, \theta - \omega\, t)$, when describing the pressure in a fixed coordinate system.

Equal to the blades' periodic position, their surrounding pressure distributions are spaced $2\pi/B$ radians apart. Hence, the pressure distribution in a reference plane near the rotor can be described as a Fourier series as in (2.1) with $a_n(r)$ and $\varphi_n(r)$ being parameters describing amplitude and phase with dependence on the radial position [13].

$$p(r, \theta, t) = \sum_{n=1}^{\infty} a_n(r) \cos\left[nB\left(\theta - \omega t\right) + \varphi_n(r)\right] \tag{2.1}$$

By observing (2.1) at a fixed angular and radial position, $p(r, \theta, t)$ reduces to (2.2):

$$p(t) = \sum_{n=1}^{\infty} a_n \cos(nB\omega\, t - \varphi_n). \tag{2.2}$$

It can be seen clearly, that the time-dependent pressure fluctuations oscillate with the blade-passing frequency (BPF) f_{BPF}:

$$f_{\mathrm{BPF}} = BN \tag{2.3}$$

and their harmonics $f_{\mathrm{BPF}n}$:

$$f_{\mathrm{BPF}n} = nBN. \tag{2.4}$$

Such periodic pressure fluctuations, which depend on the radial, as well as on the azimuthal position and spin around the duct axis are called spinning modes [13]. Two noise effects that can be described by (2.1) are the **blade thickness noise** and the **Gutin noise**. Blade thickness noise occurs due to the finite thickness of the rotor blades which causes periodic displacements of fluid mass that show acoustic monopole character. Gutin noise results from the steady blade forces which are needed to perform the required flow work and entail acoustic pressure fluctuations with dipole character [13–15].

When considering a physical ducted fan system, the tones produced by the steady rotor-fixed pressure field are not pure as indicated by (2.1). Instead, the acoustic pressure has characteristics of narrowband noise around the peaks related to the engine speed, due to imperfections in the flow field [16]. Imperfections might be the slightly different spacing of rotor blades or minor differences in the blades' geometries relating to manufacturing tolerances. Other reasons can be unwanted transient effects during operation, e.g. varying rotational speed.

Tab. 2.2. Aeroacoustic sources and characteristics in axial fans associated with the rotor, adapted from [14].

	mechanism	tonal	narrowband	broadband
rotor self-noise	blade thickness noise	■		
	Gutin noise	■		
	boundary layer noise			■
	boundary layer separation noise	■		■
	trailing edge noise (laminar BL)	■		
	trailing edge noise (turbulent BL)	■		■
	blunt TE vortex shedding	■		
	tip noise			■
turbulence ingestion (leading edge) noise				■
unsteady loading noise		■		
subharmonic tip noise			■	
rotating stall			■	
multiple pure tones		■		

Additionally to the steady acoustic pressure field described by (2.1), unsteady influences on the rotor's acoustic emissions have to be taken into account when observing the rotor acoustics of a physical ducted fan system. Flow disturbances can be divided into two main groups: disturbances produced by aerodynamic components inside the ducted fan unit itself and **ingested external disturbances** [17]. All relevant noise sources mentioned in this Chapter are summarized in Tab. 2.2, for better understanding.

Internal disturbances that interact with the rotor's pressure field are the boundary layer (BL) or turbulence effects of aerodynamic components prior to the rotor such as the inlet lib or the spinner and BL effects of the rotor itself, which are then associated with rotor self-noise. **Boundary layer noise** and **boundary layer separation noise** are general rotor self-noise effects, of which the latter occurs during the stalling of a rotor blade section. Moreover, a further acoustic sound source is **trailing edge noise** (TE) from **laminar** or **turbulent BL** in combination with resulting vortex shedding in the airfoil's wake. Another rotor self-noise mechanism is **tip noise**, which results from a tip vortex at the open blade tip as a cross-flow is developed between the suction side and the pressure side of the rotor blade. In general, rotor blades' mean wakes, wake turbulences and tip vortices are found to produce main broadband noise inside ducted fan systems by themselves [14, 15, 17, 18].

Much research has been done on the influence of ingested external disturbances, as they strongly affect acoustic behaviour. The problems first arose during the comparison between the acoustic data of jet engines gathered through both ground tests and in-flight measurements with different inflow conditions as depicted in Fig. 2.2. When ground vortices, atmospheric turbulences or other flow disturbances are ingested, they are experienced by the rotor for several revolutions due to the elongation of the flow medium in streamline direction. In conclusion, broadband noise, as well as tonal noise components, are a result of ingested external disturbances interacting with the rotor [17, 18].

Unsteady loading noise is a sound phenomenon that results from time-varying pressure

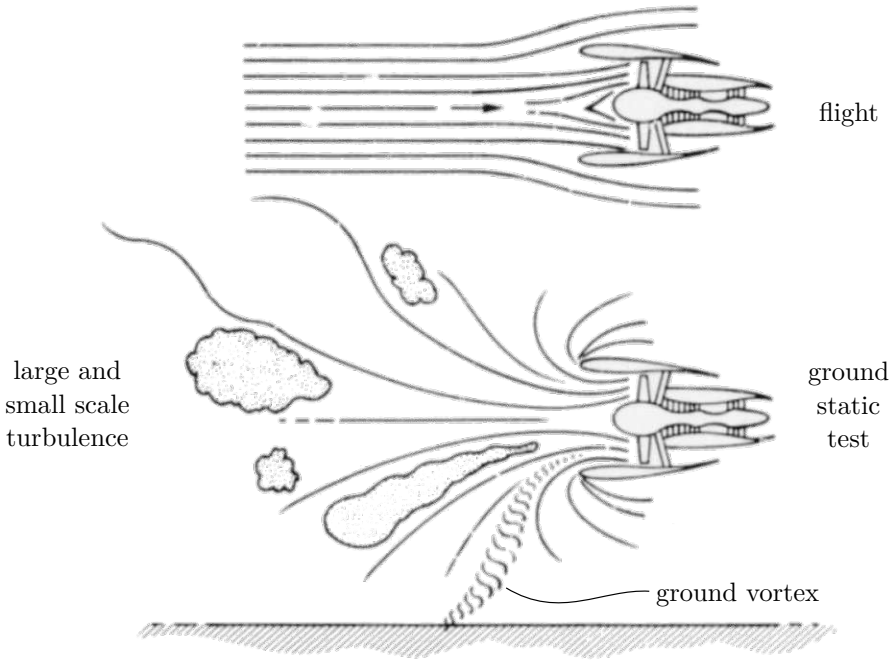

Fig. 2.2. Visualisation of turbulences affecting the noise emitted by a turbofan unit, adapted from [18].

distributions around the blades and can occur for multiple reasons such as ingested turbulences, spatially inhomogeneous inflow conditions or rotor-stator interactions, which will be closer examined in Chap. 2.1.2. Another tip noise mechanism is introduced by the **subharmonic tip noise**, which can be noticed by subharmonic narrowband humps that arise in the acoustic spectrum. It occurs due to flow structures in the region close to the blade tips, which interact with the blades and rotate at an angular velocity different to that of the fan itself. **Rotating stall** describes a phenomenon of BL separations in the deep stall region of axial fans. When a fan blade stalls, the volume flow is partially halted from passing that blade, which forces it to pass the adjacent blades, resulting in stalling conditions for further blades [14, 19].

When rotor tip speeds go supersonic, a phenomenon occurs that drowns out the amplitudes of all other acoustic effects generated by the rotor. The so-called multiple pure tones (MPT) have their origin in the rotor-locked, leading edge shocks produced by the rotor blades' supersonic velocities in the region close to the blade tips [17]. The reason for the MPT's rather extended frequency range are spatial non-uniformities in the rotor's pressure field, which arise through disturbances and manufacturing tolerances and cause the supersonic shocks to behave slightly differently for each blade [20, 21].

Noise reduction by rotor design

Different blade design approaches have been taken in order to reduce the acoustic pressure emitted by the rotor. The number of blades can be increased to lower the sound pressure levels (SPL) resulting from steady blade loading (Gutin noise) [19]. Additionally, irregular

blade spacing has been proven to result in a spreading of the sound energy's tonal components over a wider frequency band, and thus improving the noise characteristics emitted from a psychological point of view [5, 19, 22].

Generally, a reduction in tip clearance between rotor and duct results in a noise reduction in ducted fans. As an argument is cited, that the smaller the tip clearance is made, the more accurately the rotor has to be centred with the duct axis, so that the tip sees a uniform boundary layer [19].

The forward and backward lean of rotor blades (see Fig. 2.3) has been evaluated, with both axial directions shown to provide a noise reduction due to phasing of turbulence ingestion noise along with the blades' leading edge (LE). Positive and negative sweep has the same purpose as forward and backward in terms of noise reduction through phasing of the unsteady blade forces evoked by a non-uniform inlet flow [14, 19]. Leading edge serrations can further improve the fan rotor's acoustic behaviour under free inflow conditions. However, under inflow conditions with high turbulence intensities, an increase in the SPL was even detected [14].

2.1.2 Rotor-stator interaction

Stators are used inside a ducted fan system to compensate for the rotation in the flow due to the rotor's pressure field. To fulfil this purpose, the stator vanes' cross-sections are usually designed as airfoils and experience similar self-noise mechanisms as the rotor (Tab. 2.2) with exception of blade thickness, Gutin and tip and noise due to the absence of rotation and tip clearance.

Often the stators are also used as a form of rigid suspension for the rotor to avoid the use of turbulence generating struts. In single-stage axial flow fan systems, the stator can either be positioned upstream or downstream of the rotor. As depicted earlier in Fig. 2.1, most modern axial flow fans are designed with a downstream stator, resembled through the so-called outlet guide vanes (OGV), as studies have shown significantly lower SPL for the resulting rotor-stator interaction compared to upstream stator installations [23].

The prevailing pressure gradients around the fan blades force the flow medium to flow around blades and vanes with the main velocity component in the axial direction and minor components in the radial and tangential direction. Subsequently, a non-constant pressure field is developed around the stator vanes, that is rigidly attached to the stator. As each rotor blade passes a stator vane, the rotor's pressure field interacts with the stator's pressure field and an impulse of pressure is developed with magnitude and shape being dependent on the particular blades and vanes involved. With every particular blade-vane interaction being equivalent, a periodic waveform of the frequency $V \cdot f_{\mathrm{BPF}}$ would result. Should B and V have a highest common factor k, then some pulses occur simultaneously and the basic frequency is $\frac{V\, f_{\mathrm{BPF}}}{k}$. With imperfections in the rotor and stator configuration the main noise frequencies due to rotor-stator interaction are also at f_{BPF}, N and their respective harmonics [13, 16].

A general expression of the acoustic pressure fluctuations in a reference plane near the rotor-stator interaction is given by (2.5):

$$p(\theta, t) = \sum_{n=1}^{\infty} \sum_{m=-\infty}^{\infty} V a_{mn} \cos\left[m\theta - nB\omega t + \varphi_{mn}\right] \tag{2.5}$$

where m is limited to the following values:

$$m = nB + kV, \quad k = \ldots, -1, 0, 1, \ldots \tag{2.6}$$

In (2.6), m describes the number of lobes a spinning pattern obtains. Every m-lobe spinning pattern spins at $\omega_m = \frac{2\pi f_{\mathrm{BPF}n}}{m}$ rad/s of angular speed. As described earlier for the rotor-fixed pressure field's acoustic emissions for a physical ducted fan system, the tones resulting from the rotor-stator interaction are not pure either, but also have characteristics of narrowband noise. Reasons can be any kind of flow field imperfections or transient operation effects [16].

Flow field disturbances have additional effects on the acoustic behaviour of the rotor-stator interaction. The disturbances that emerge internally and are created mainly by the rotor blades are its wakes and the tip vortices. A thorough description of rotor produced disturbance flow fields in accordance with midspan wakes and tip vortices has to be made in order to gain detailed insight into the exact flow mechanism and its acoustic consequences [17].

Noise reduction by stator design

There has been early research work on the noise produced by rotor-stator interaction in relation to the vane design, vane spacing and axial separation between blades and vanes. Two vane design parameters for efficient sound reduction in the rotor-stator interaction are lean and sweep angle, which are shown in Fig. 2.3. The purpose of introducing sweep and lean angle to vane design is the phasing of the rotor-stator interaction over the blades TE and the vanes' LE. [19, 24–26]

Other possibilities for reducing rotor-stator interaction noise are the irregular spacing of individual vanes and stepped vanes with different chord lengths over their radial extent to further increase the interaction's phasing [19]. Moreover, acoustic emissions can be controlled

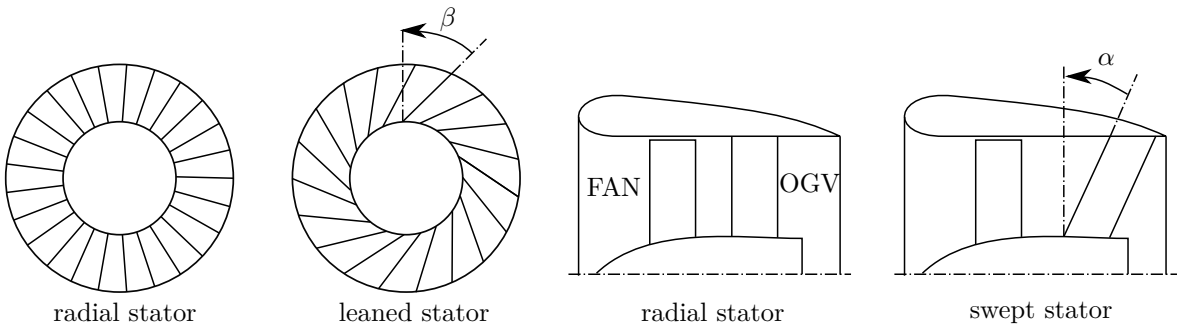

Fig. 2.3. Definition of sweep and lean angle, adapted from [24].

via the number of blades and vanes, which will be examined closely in Chap. 2.2.2.

Furthermore, studies have resulted in a recommendation in terms of the axial separation of both rows at $d_x = 40\,\%$ of the rotor's chord, which sufficiently reduces the effect of potential interaction. On the other hand, the effect due to rotor blades' wakes decreases only gradually with increasing d_x [19, 27].

2.1.3 Flow wake

For ducted fans operating subsonically, where the exhaust velocity does not exceed the local speed of sound, the noise due to the mixing of the flow wake with the surrounding atmosphere is the flow wake's main acoustic source aside from other possible flow effects such as vortex shedding. As the eddies that occur due to the turbulent mixing process differ widely from each other, the frequency spectrum is rather broad and shows clear broadband noise characteristics. The only trends the eddies comply with are an increase in size and a decay of intensity downstream of the duct outlet as the flow wake's velocity decreases [4].

In regard to the directivity pattern of a subsonic flow wake's mixing noise, a peak in the SPL $L_\mathrm{p}(\theta)$ occurs in the middle of the wake's rear arc ($90° < \theta < 180°$), as shown in Fig. 2.4. The forward arc ($\theta < 90°$) is less affected by acoustic pressure fluctuations through the mixing noise emitted and can be described as decaying towards the duct's outlet section [4, 19].

Previous research that already stated broadband noise generation can be caused by the shear stress of the mixing process in flow wakes found a theoretical relation between the mixing process's acoustic intensity and exhaust velocity. The law resulting from the above-mentioned research is known as the eighth power law and indicates that acoustic intensity scales with the eighth power of the flow wake's mean velocity [28]. Although the law might be fulfilled under willing circumstances, it has also been observed that there are rather big discrepancies from the law's predictions in various other research, especially at high and low velocities [4].

Noise reduction by exhaust section design

Apart from reducing the exhaust flow's mean velocity, which comes with decreased thrust for unchanged duct diameters (see Chap. 2.4.1), the mixing noise can be diminished by improving

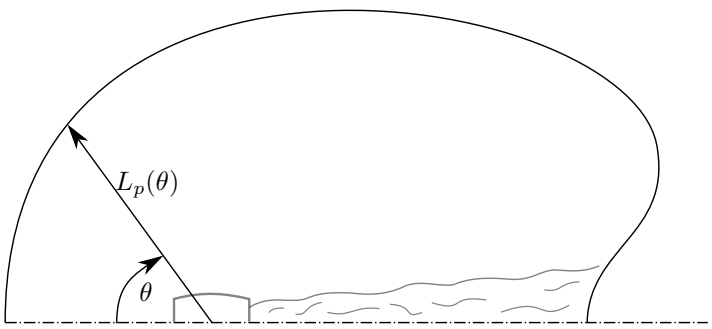

Fig. 2.4. Polar directivity pattern of flow wake's acoustic pressure emissions of a subsonic jet exit speed, adapted from [19].

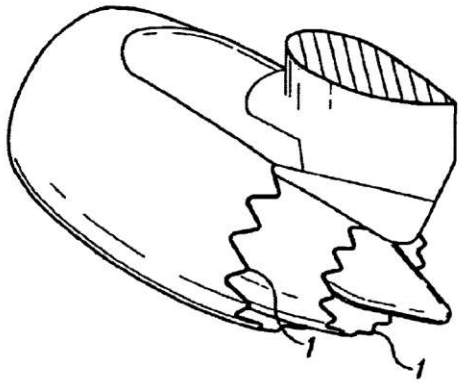

Fig. 2.5. Exhaust end pipe serrations (1) for reduced exhaust flow noise, from [29].

the flow wake's mixing process. Modifications of the exhaust end pipe as shown in Fig. 2.5 are called chevrons and help to control the mixing of the exhaust flow with the ambient atmosphere. The use of chevrons results in a more uniform flow in the downstream direction of a ducted fan system. However, thrust is decreased as an unwanted by-product [4, 29].

2.1.4 Electric powertrains

Acoustic emissions relating to electric powertrains as depicted in Fig. 2.1 can result from either the motor or the power converter. The following observation will be limited to electronically commutated motors (ECM) and the according electronic speed controllers (ESC) to narrow down the variety of motor and converter types. The main causes of their noise emissions are of an aeroacoustic (aeroac.), structural (struct.), electromagnetic and electrical (el.mag. & el.) nature, whereby the latter two are transmitted as structure borne sound initially [1, 30]. The different sources of mechanism for acoustic emissions from the electric powertrain are listed in Tab. 2.3.

Typically, power electronic components experience a rather noticeable amount of power dissipation, depending on their operating efficiency. The lost electric power, which is dissipated into heat, must leave the electric components via heat transmission, which may

Tab. 2.3. Acoustic sources and characteristics in axial fans associated with the electric powertrain.

	mechanism	ECM	ESC	tonal	broadband
aeroac.	boundary layer noise	■	■		■
	vortex shedding	■	■	■	
	cavity resonance	■	■	■	
struct.	bearing noise	■		■	■
	ECM rotor unbalance	■		■	
	structural modes	■		■	
el.mag. & el.	tangential Lorentz force	■		■	
	normal Lorentz force	■		■	
	cogging torque	■		■	
	torque ripple	■		■	
	switching frequency		■	■	

require adequate cooling infrastructure to overcome overheating issues. In certain instances, placement of the electric components inside the flow field can contribute positively to heat transmission by taking advantage of so-obtained forced convection. When either of the components is immersed into the flow field, the problems of forward- and/or backward-facing step - respectively flow around an obstacle - emerge. Therefore, acoustic pressure fluctuations can result in aeroacoustic reasons for noise due to **BL turbulences** and **vortex shedding**. Furthermore, **cavity resonances** can be an issue, especially regarding the ECM's air gap between its rotor and stator [30].

Structural sources for structural vibration can result from the motor itself and have their origin in static or dynamic **rotor unbalance**, **bearing noise** and **structural modes**.

Electromagnetic sources are the variations in exciting forces and resulting torques that cause vibration and the propagation of acoustic waves. The exciting electromagnetic forces and torques of an ECM can be divided into local forces and global torques, which result from the electromagnetic interaction of the rotor's permanent magnets' magnetic field and the moving electric charges in the stator known as the Lorentz force [31]. Local forces are the **normal** and the **tangential Lorentz force** components which are dependent on the permanent magnets' magnetic field, the stator coil design, the supply current and air gap permeances. Global torques are represented by the **torque ripple** and the **cogging torque**. Torque ripple is the difference of maximum and minimum output torque due to periodic changes of the local forces during one electric cycle, whereas the cogging torque describes a parasitic torque due to the interaction of the rotor's permanent magnets and the stator slots [1,30–32]. Predominant sound frequencies due to the electromagnetic sources are dependent on the ECM's rotational speed N and the motor's poles. The electromagnetic frequency of the local forces f_{LF} can be calculated using the number of motor poles p in (2.7)

$$f_{\mathrm{LF}} = pN \tag{2.7}$$

and its harmonics $f_{\mathrm{LF}n}$:

$$f_{\mathrm{LFn}} = npN. \tag{2.8}$$

The final major acoustic source from the electric powertrain is the ESC's **switching frequency**. It is a high-frequency switching noise (multiple kHz), depending on the ESC and its settings, which shows tonal characteristics and is generally independent of the ECM's operating conditions [30].

2.2 In-duct transmission

Before noise that is generated inside a ducted fan system can radiate to the far-field it has to propagate through the duct towards the inlet section and the outlet section. The acoustic pressure fluctuations have to propagate through different kinds of cross-sections and pass stator vanes or rotor blades depending on the location of the acting sound source and the

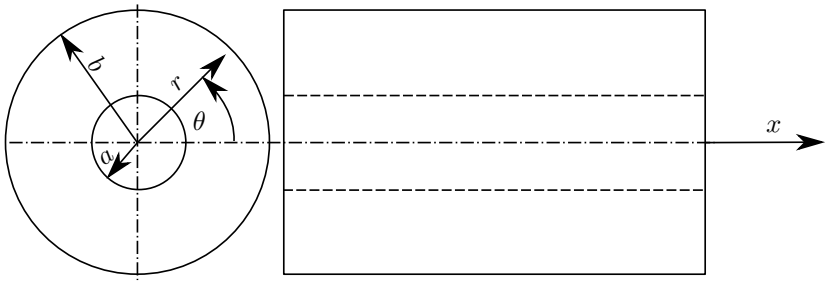

Fig. 2.6. Concentric cylindrical ducts showing dimension variables.

ducted fan's design. In order to improve clarity, the in-duct transmission is divided into the acoustic propagation between two concentric cylindrical ducts and a resulting design proposal to reduce propagating acoustic modes.

2.2.1 Concentric cylindrical ducts

A simplified geometric model of propagation space is considered to discuss the propagation of waves inside a ducted fan system. As regular ducted fan systems are composed of an approximately cylindrical duct on the outside and approximately cylindrical, concentric components[2] on the inside, the simplified propagation space is confined by two concentric hard-walled cylinders as shown in Fig. 2.6. When solving the acoustic wave equation for the chosen propagation space without considering a mean flow, Bessel functions can be used to obtain the resulting pressure fields for an acoustic (m, μ)-mode inside the ducts [13]. The respective field of the mode's acoustic pressure $p_{m\mu}(r, \theta, x, t)$ is described in (2.10) to (2.13) with m being the number of the mode's circumferential lobes and μ being the number of the respective Bessel function's zeros in radial direction. The two resulting cases of a mode's pressure field (2.10) and (2.12) depend on the relationship between the mode's circumferential Mach number M_m and the critical Mach number M_m^*, where M_m can be expressed by a modes angular velocity Ω_m and the local speed of sound c:

$$M_m = \frac{b\omega_m}{c} \tag{2.9}$$

When the observed (m, μ)-mode's circumferential Mach number does not exceed the critical Mach number, (2.10) describes its acoustic pressure field:

$$p_{m\mu}(r, \theta, x, t) = a_{m\mu} p_\mu(r) \cos\left[m\left(\theta - \omega_m t\right) + \varphi_m\right] \mathrm{e}^{-k_{x\mu} x} \tag{2.10}$$

where the exponential decay rate $k_{x\mu}$ is calculated as follows:

$$k_{x\mu} = \frac{m}{b}\sqrt{{M_m^*}^2 - {M_m}^2}, \quad M_m^* = \left(\frac{k_{m\mu}^{\prime(\sigma)}}{m}\right). \tag{2.11}$$

Taking a closer look at (2.10) brings forward the pressure field decaying character with increasing axial coordinate x. With decreasing M_m, the pressure field decays exponentially

[2] e.g. Spinner, electric motor housing, turbine

Tab. 2.4. Critical circumferential tip Mach number M_m^*, from [13].

m	$\sigma = 0$	$\sigma = 0.25$	$\sigma = 0.5$	$\sigma = 0.75$
1	1.84	1.64	1.36	1.15
2	1.53	1.50	1.34	1.15
4	1.33	1.33	1.29	1.14
8	1.21	1.21	1.20	1.14
16	1.13	1.13	1.13	1.12
32	1.08	1.08	1.08	1.08

over axial distance. As can be seen in (2.11), the critical Mach number depends on the characteristic number $k_{m\mu}^{'(\sigma)}$ which is associated with the Bessel functions. The characteristic number itself depends on the hub-tip ratio $\sigma = \frac{a}{b}$, m and μ.

When the critical Mach number is exceeded by a spinning mode's tip Mach number, (2.12) and (2.13) define its acoustic pressure field $p_{m\mu}(r, \theta, x, t)$ as follows:

$$p_{m\mu}(r, \theta, x, t) = a_{m\mu} p_\mu(r) \cos\left[m\left(\theta - \omega_m t\right) + k_{x\mu} x + \varphi_m\right] \tag{2.12}$$

where $k_{x\mu}$ is calculated by (2.13):

$$k_{x\mu} = \frac{m}{b}\sqrt{{M_m}^2 - {M_m^*}^2}, \quad M_m^* = \left(\frac{k_{m\mu}^{'(\sigma)}}{m}\right). \tag{2.13}$$

Closer examination of (2.12) reveals the propagating nature of those spinning modes, as no decay occurs with increasing axial coordinate x. The only influence of the Mach numbers' difference results in the change of phasing of the propagating modes.

To obtain a better insight into the critical tip Mach number's range of values, its values are presented in Tab. 2.4 for the Bessel function with no zeros ($\mu = 0$) and in dependence on discrete values of m and σ [13]. Through the information obtained from Tab. 2.4, it can be seen that only supersonic circumferential tip Mach numbers of spinning modes exceed the critical Mach number needed for a mode to propagate inside the duct. With increasing σ and m, the critical Mach number converges towards 1 which limits unattenuated propagation to the supersonically rotating spinning modes. Following the argumentation from Chap. 2.1.1, the spinning modes resulting from the steadily rotating pressure field of a rotor with subsonic tip speed cannot propagate but decay inside the duct, depending on the difference between M_m and M_m^*. To show the decay of a selection of modes, Fig. 2.7 shows the decay rates of different values of m and σ. The spinning modes that result from the rotor-stator interaction can have a variety of circumferential frequencies as discussed in Chap. 2.1.2 and therefore enable the occurrence of modes with supersonic tip Mach numbers in subsonic ducted fans which then propagate according to (2.12) [13, 33].

2.2.2 Tyler and Sofrin Rule

Tyler and Sofrin were able to state a selection rule for the number of rotor blades B and stator vanes V, with rotor-stator interaction identified as the main acoustic source in subsonic ducted fans due to the propagation character of its spinning modes [13].

With selection of B and V to cut off the nth harmonic according to the inequality (2.14) for tip speeds smaller than the speed of sound [34]:

$$n\,B \leq |m| = |nB + kV| \tag{2.14}$$

(2.14) holds because if fulfilled for an nth harmonic, the resulting spinning modes obtain an angular speed of $nB\,\omega/m$ rad/s, which will result in a tip speed less than the rotor's tip speed. The relevant values of kV that need to be observed when choosing B and V are in the interval $-2nB < kV < 0$. If this condition is satisfied for $k = -1$, it is satisfied for any k. Therefore, the final condition is as follows: $V \geq 2nB$. As this condition is very conservative, a smaller V can be selected in case the rotor's tip Mach number is significantly smaller than 1.

As illustrative example, a single-stage fan system with $B = 7$ rotor blades and $V = 15$ stator vanes is considered, which applies to the above condition and will result in the following numbers of m for $n = 1$ and $n = 2$:

$$\begin{aligned} \text{for } n = 1: &\quad m = \ldots, -23, -8, 7, 22, \ldots \\ \text{for } n = 2: &\quad m = \ldots, -16, -1, 14, 29, \ldots \end{aligned}$$

where indeed all modes of the first harmonic are cut-off for subsonic rotor tip speeds and only one counter rotating mode remains ($m = -1$) of the second harmonic.

Two mechanisms that further hinder the propagation of spinning modes upstream to a ducted

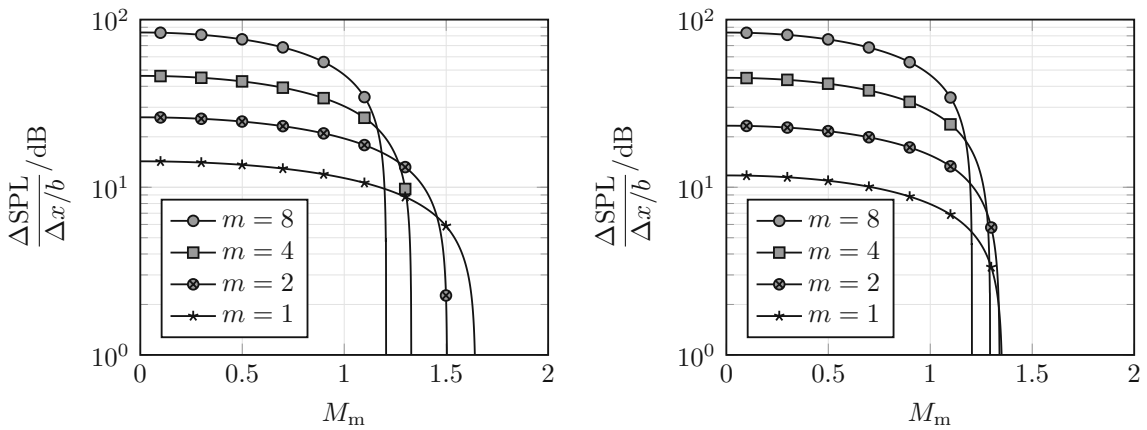

(a) Decay for $\sigma = 0.25$ **(b)** Decay for $\sigma = 0.75$

Fig. 2.7. Decay of different m-lobed modes for $\mu = 0$ as function of the tip Mach number.

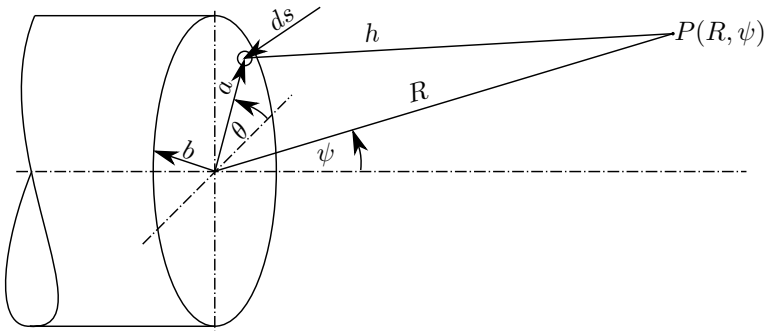

Fig. 2.8. Cylinder's open face with coordinates.

fan's inlet section are the mean flow inside the unit and the moving rotor blades, which act as a physical barrier. The blades behave as a series of Venetian blinds that appear open or shut to the upstream propagating spinning mode, depending on the angle and direction of its spiral movement.

The proposed rule does not account for flow irregularities as its definition is based on radially symmetric conditions without any flow distortions, ingested or due to internal generation.

2.3 Far-field radiation

The far-field radiation from a ducted fan comes mainly from both the duct's inlet and outlet section. As mentioned in Chap. 2.2, the conditions inside a ducted fan system do not benefit the propagation of some spinning modes upstream. Mathematically, it is useful to simplify the actual duct's termination geometry as the open end of a cylinder without mean flow. Therefore, the acoustic pressure at the open face is best described in dependence on the characteristic Bessel function of first kind $J_m(k_{m\mu}\, r)$ for a single full-volume cylinder [13].

$$p_{m\mu}(r,\theta,t) = a_{m\mu} J_m(k_{m\mu} r) \cos\left(m\theta - B\omega t\right) \tag{2.15}$$

The spherical coordinates R and ψ, which are used to describe a location in the far-field, are shown in Fig. 2.8. The preceding definitions are then used to define the acoustic pressure fluctuations $P_{m\mu}(R,\psi,t)$ at a point in the far-field by the integration of the pressure contribution from a differential element ds over the duct's surface. The resulting relations (2.16) and (2.17) reveal the directivity pattern for a general (m,μ)-mode:

$$P_{m\mu}(R,\psi,t) = \frac{A_{m\mu} \cos\left[\frac{2\pi f_{\mathrm{BPF}}}{c}(R-ct)\right] \sin\psi\, Q}{R\left[{k_{m\mu}}^2 - \left(\frac{2\pi f_{\mathrm{BPF}}}{c}\right)^2 \sin^2\psi\right]} \tag{2.16}$$

where

$$Q = J_{m-1}\left(\frac{2\pi f_{\mathrm{BPF}}}{c} b \sin\psi\right) - J_{m+1}\left(\frac{2\pi f_{\mathrm{BPF}}}{c} b \sin\psi\right). \tag{2.17}$$

The directivity pattern for a spinning mode depends strongly on m and μ but the mode's circumferential tip Mach number M_m is the most important factor involved. With

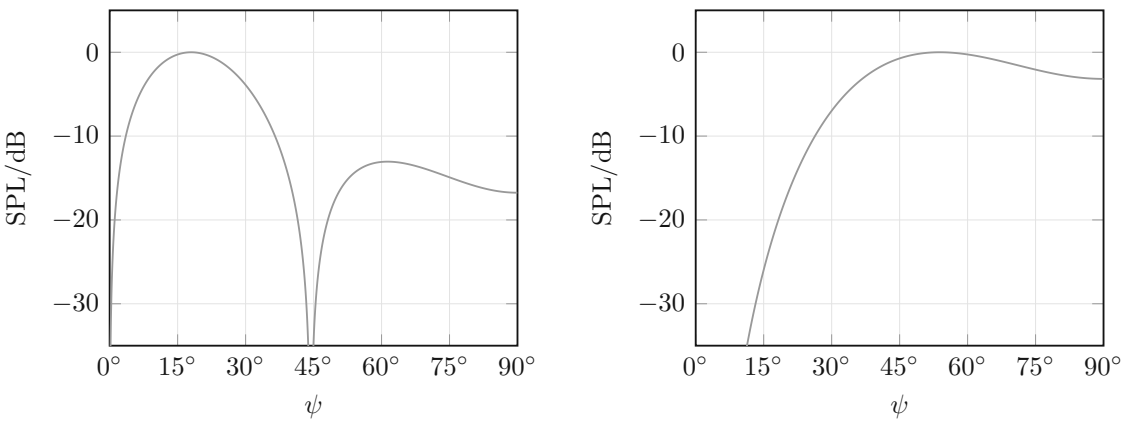

(a) Mode with $m = 1$ and $M_\mathrm{m} = 4.14\,M_\mathrm{m}^*$

(b) Mode with $m = 4$ and $M_\mathrm{m} = 1.44\,M_\mathrm{m}^*$

Fig. 2.9. Radiation pattern of spinning modes from a cylindrical duct to the far-field.

increasing tip Mach numbers, the directivity pattern theoretically experiences angles at which the acoustic pressure fluctuations even vanish completely for a spinning mode, which can be seen from the two calculated radiation patterns in Fig. 2.9. This accounts for the duct's axial direction for every spinning mode with the only exception being a plane wave radiating from the duct's open face. There has been successful research during which spinning modes have been examined and predicted by far-field measurements solely using a ducted fan's directivity patterns. The equations above were found promising in the subsonic region of operation. However, for the supersonic operation of a ducted fan, a calculation model that considers a mean flow inside the duct delivered good results [35, 36].

2.4 Similarity laws

2.4.1 Thrust scaling

The thrust obtained by a ducted fan system relies strongly on the geometric properties of the rotor and stator design and its operating conditions. The simplified relationship (2.18) for the aerodynamic thrust F_T, which is known as the momentum theory, can be given as function of the converted power P_T, the rotor area A_Rotor and the flow medium's density ρ_0.

$$F_\mathrm{T} = \sqrt[3]{P_\mathrm{T}^2 2\rho_0 A_\mathrm{Rotor}} \propto \sqrt[3]{{d_\mathrm{Rotor}}^2} \tag{2.18}$$

In (2.18) can be seen that for unchanged powering conditions, the thrust scales with the third root of the rotor area, or with the square of the third root of the rotor diameter d_Rotor. Therefore, fan efficiency genuinely improves with an increasing rotor area.

Additionally, as the thrust can be associated with the volume flow $\dot{V}_0$ and the flow's mean velocity $\bar{u}$ according to (2.19), the thrust can be said to scale with the square of $\bar{u}$ for a constant rotor area A_Rotor [12].

$$F_\mathrm{T} = \rho_0 \dot{V}_0 \bar{u} = \rho_0 A_\mathrm{Rotor} \bar{u}^2 \propto \bar{u}^2 \tag{2.19}$$

2.4.2 Sound power level scaling

The scaling of the aerodynamically generated sound power P can be expressed as (2.20) as being dependent on a characteristic length L and a characteristic flow velocity u with c_0 being the speed of sound:

$$P \propto \rho_0 L^2 u^3 \left(\frac{u}{c_0}\right)^m \tag{2.20}$$

where the Mach number exponent m is calculated by (2.21):

$$m = (n_{\text{dim}} - 3) + (2e - 1)\,. \tag{2.21}$$

In (2.21), n_{dim} resembles the dimensions of sound propagation ($n_{\text{dim}} = 3$ for free field conditions) and the source-dependent exponent $e = 1$, 2 and 3 for monopoles, dipoles and quadrupoles respectively [19]. This circumstance emphasizes the rather wide variation of the velocity exponent for sound power scaling depending over the acoustic source's radiation characteristics and propagation conditions.

2.4.3 Scaling from a model to a full-size fan

For an identical working fluid and an equal rotor tip speed, which results in constant Strouhal (St) and Helmholtz (He) numbers, the scaling from a model size fan to a full-size version is rather simple [19]. For the total sound power, P can be expressed by (2.22), where u_{tip} denotes the tip speed and M_{tip} denotes the tip Mach number:

$$P = C\,\rho_0 {u_{\text{tip}}}^2 {M_{\text{tip}}}^{1+2\epsilon} {d_{\text{Rotor}}}^2 \tag{2.22}$$

with ϵ being the tip speed exponent, which has to be determined for a specific fan model. The tip speed exponent can even vary for one fan model depending on whether the measuring location is at the duct inlet or outlet section.

For the total sound power level in dB, (2.23) can be found when transforming (2.22) with the respective reference values for the tip speed, diameter, density, and speed of sound $u_0 = 1\,\text{m/s}$, $d_0 = 1\,\text{m}$, $\rho_\infty = 1.19\,\text{kg/m}^3$, and $c_\infty = 343\,\text{m/s}$ for air at $20\,°\text{C}$:

$$L_W = L_{W\text{s}} + 10(4 + 2\epsilon)\,\lg\frac{u_{\text{tip}}}{u_0} + 20\,\lg\frac{d_{\text{Rotor}}}{d_0} + 10\,\lg\frac{\rho_0}{\rho_\infty} - 10(1 + 2\epsilon)\,\lg\frac{c_0}{c_\infty}. \tag{2.23}$$

(2.23) can now be transformed to find the desired sound power level difference between two dimensionally similar axial fans (2.24):

$$L_{W2} - L_{W1} = 10(4 + 2\epsilon)\,\lg\frac{u_{\text{tip2}}}{u_{\text{tip1}}} + 20\,\lg\frac{d_{\text{Rotor2}}}{d_{\text{Rotor1}}} + 10\,\lg\frac{\rho_{02}}{\rho_{01}} - 10(1 + 2\epsilon)\,\lg\frac{c_{02}}{c_{01}}. \tag{2.24}$$

Chapter 3

Aero-engine liners

Secondary measures can be taken to further minimize the radiated sound from a ducted fan into the far-field, in addition to noise reduction through manipulation of the acoustic source mechanisms as described in Chap. 2. Therefore, the sound waves emitted have to be influenced during their propagation path by so-called acoustic linings to obtain the desired attenuation.

As most aircraft parts, aero-engine liners must meet strict requirements in terms of weight and volume characteristics. Moreover, they must obtain capabilities to attenuate a wide range of frequencies from different tonal and broadband noise due to varying engine operating conditions. A further difference to classic linings used for room acoustics, for example, are the harsh conditions under which the devices have to function when installed in an aero-engine. High flow velocities and high temperatures, in the case of a combustion powered engine, need to be endured by aero-engine liners. Additionally, manufacturability and maintainability requirements have to be fulfilled to allow a long term use under absolutely safe conditions, as engines are one of the aircraft's critical components. The requirements that have to be met by aero-engine liners are summed up in Fig. 3.1.

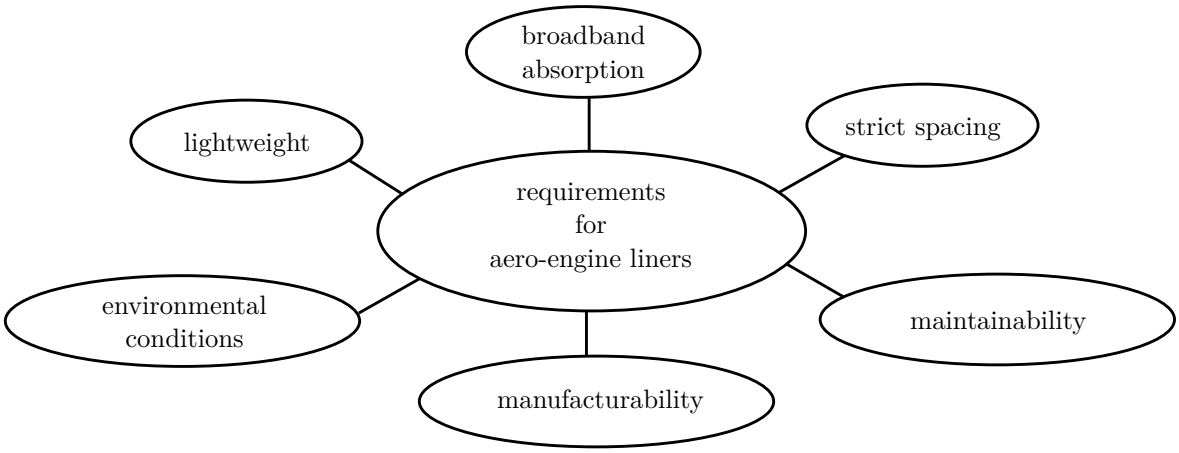

Fig. 3.1. Operating conditions of absorber linings for the use in aero-engines.

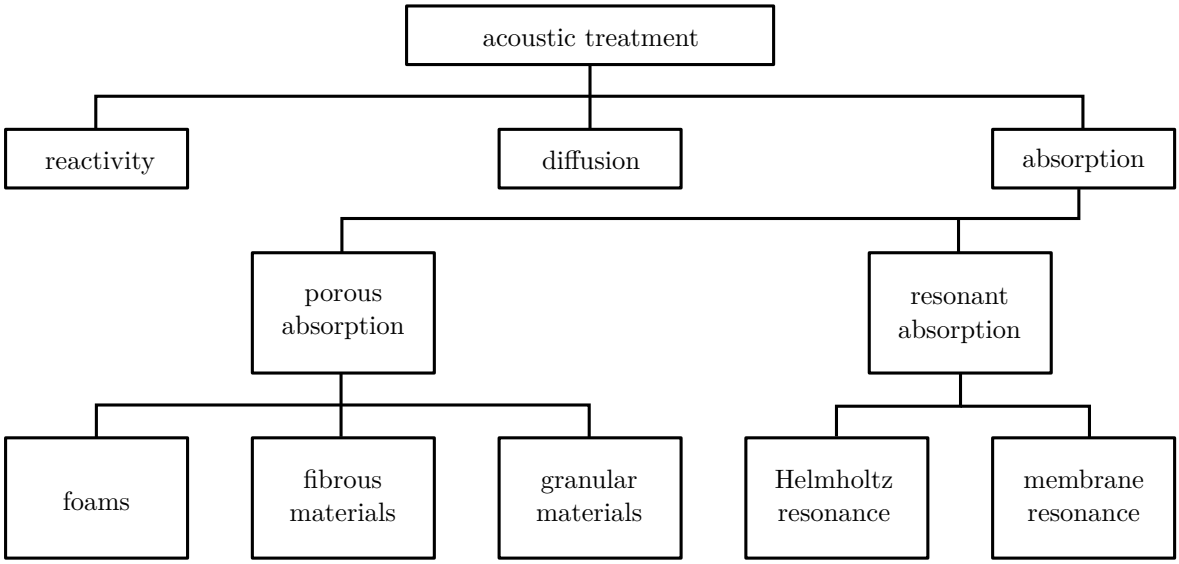

Fig. 3.2. Outline of mechanisms for acoustic treatment.

Possible sound reduction at an observer point can be achieved through diffusive, reactive or absorptive mechanisms, where only absorption actively reduces sound energy.

Diffusive and reactive mechanisms exploit the reflection characteristics of sound through surface manipulations or varying cross-section sizes, respectively. In the case of axial-flow compressors, which generate thrust by the accelerated high-velocity flow inside cylindrical boundaries, diffusive elements would generate rather high pressure drops that reduce the overall efficiency. Moreover, noise-generating turbulence might be induced by such sound treatment devices [37].

Reactive silencing results from reflections caused by the flow medium's sudden impedance changes. Those changes in impedance are invoked by discontinuous cross section profiles in flow direction and can be created in combination with absorptive attenuation [38–41]. The sound reduction mechanisms discussed are illustrated in Fig. 3.2

Attenuation devices that actively decrease the sound energy emitted by acoustic sources are called **absorbers** and can be divided into two main groups which are **porous** and **resonant** absorbers. Both groups differ from each other via their absorption principles and will be discussed more closely in Chap. 3.2 and Chap. 3.3

3.1 Absorption fundamentals

To mathematically describe the behaviour of acoustics in a convenient way, the acoustic pressure p_a and the acoustic particle velocity v_a for a plane wave may be expressed as complex values in relation to the time t, a one-dimensional coordinate x and the angular frequency $\omega = 2\pi f$ as in (3.1) [34, 41–43]. :

$$p_\mathrm{a} = \hat{p}\mathrm{e}^{j(\omega t - kx)}, \quad v_\mathrm{a} = \frac{\hat{p}}{\rho_0 c}\mathrm{e}^{j(\omega t - kx)} \tag{3.1}$$

with $\hat{p}$ being a constant describing the wave's magnitude and k being the characteristic wavenumber:

$$k = \frac{\omega}{c} = \frac{2\pi f}{c}. \tag{3.2}$$

The medium's density and speed of sound are denoted by ρ_0 and c respectively. To link the acoustic pressure and acoustic particle velocity of a plane wave in a uniform medium, a property called characteristic impedance z_c is used, as derived in (3.3).

$$z_\mathrm{c} = \frac{p_\mathrm{a}(t,x)}{u_\mathrm{a}(t,x)} = \frac{\hat{p}\mathrm{e}^{j(\omega t - kx)}}{\frac{\hat{p}}{\rho_0 c}\mathrm{e}^{j(\omega t - kx)}} = \rho_0 c \tag{3.3}$$

3.1.1 Single interface

For the further characterization of absorbers, the case of a plane wave coinciding with an interface between two different media without backings is considered as depicted in Fig. 3.3. The behaviour of an incident wave acting on an interface can be described by the surface impedance z_s, the reflection coefficient R and the absorption coefficient α. The surface impedance z_s is the ratio of the acoustic pressure and acoustic particle velocity perpendicular to the respective surface. In the case of an interface between two infinite media the surface impedance is equal to the characteristic impedance of layer 1 $z_\mathrm{s} = z_\mathrm{c1}$. It is needed to compute the reflection coefficient R in (3.4), which is the ratio of the reflected pressure wave p_r to the incident pressure wave p_i and generally depends on the angle of incidence ψ.

$$R = \frac{p_\mathrm{r}}{p_\mathrm{i}} = \frac{z_\mathrm{s}\cos\psi - z_\mathrm{c}}{z_\mathrm{s}\cos\psi + z_\mathrm{c}} \tag{3.4}$$

The absorption coefficient α denotes the ratio of absorbed energy P_abs and incident energy P_inc inherited by an acoustic wave that interacts with an absorber and can be described in dependence of the reflection coefficient R as in (3.5)

$$\alpha = \frac{P_\mathrm{abs}}{P_\mathrm{inc}} = 1 - |R|^2 = 1 - \left|\frac{z_\mathrm{s}\cos\psi - z_\mathrm{c}}{z_\mathrm{s}\cos\psi + z_\mathrm{c}}\right|^2 \tag{3.5}$$

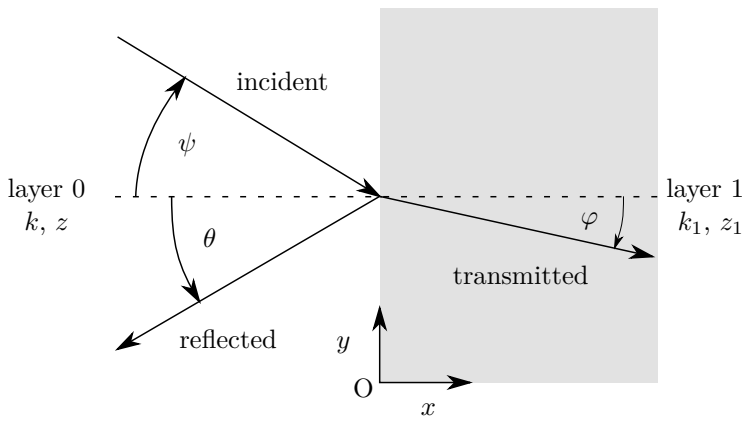

Fig. 3.3. Propagation properties for a plane wave coinciding at an interface between different media, adapted from [41].

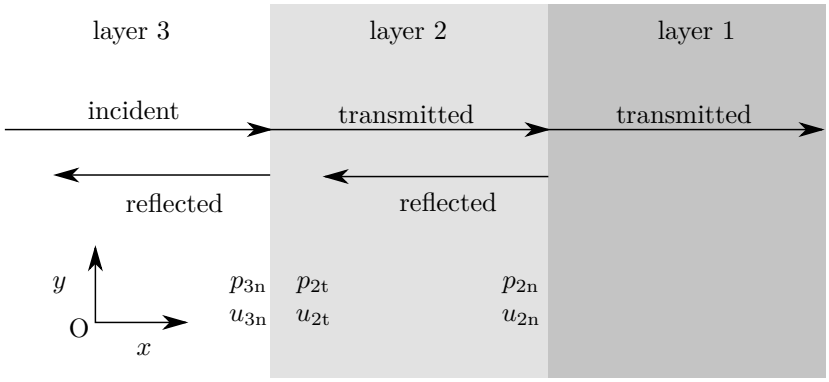

Fig. 3.4. Propagation properties for a plane wave coinciding at multiple interfaces between different media, adapted from [41].

3.1.2 Multiple interfaces

In order to consider the case of acoustic plane wave propagation through multiple layers of different media, a perpendicular incidence angle ($\psi = 0$) is considered. The propagation pattern for three layers is presented in Fig. 3.4 and can be extended likewise. Pressure and velocity boundary conditions at the interfaces have to be considered to finally reach expression (3.6) of the wall impedance for the second interface:

$$z_{s2} = \frac{-j z_{s1} z_{c1} \cot(k_2 d_2) + (z_{c2})^2}{z_{s1} - j z_{c2} \cot(k_2 d_2)} \tag{3.6}$$

with the respective indices of z_s, z_c, k and d for the respective layers and interfaces [41].

3.2 Porous absorbers

Porous sound absorption is achieved when sound waves are transmitted through a porous material, which qualifies for this purpose. Such porous materials need interconnected pores, which allow sound propagation solely through the gaseous or fluid medium. The difference between open- and closed-pore structures is depicted in Fig. 3.5. The main forces acting on the medium are friction forces at the pore walls. Respectively, sound absorption does not mainly happen through material vibration but the viscous BL and thermal effects in the interconnected paths. As the BL size resulting from acoustic particle velocities is smaller than one millimetre in the range of audible frequencies, the pores' size should lay in that order of magnitude to maximize the absorber's efficiency. Momentum losses inside the porous materials occur due to changes in the flow direction, which are induced by irregular pore structure.

The simple case of a single uniform porous absorber plate of thickness d with a rigid backing is considered to obtain the behaviour of a porous absorber. This case is a special form of the multiple layer approach from Chap. 3.1.2 with the surface impedance of the rigid backing being infinite $z_{s1} = \infty$. The surface impedance of the absorber front for a perpendicularly

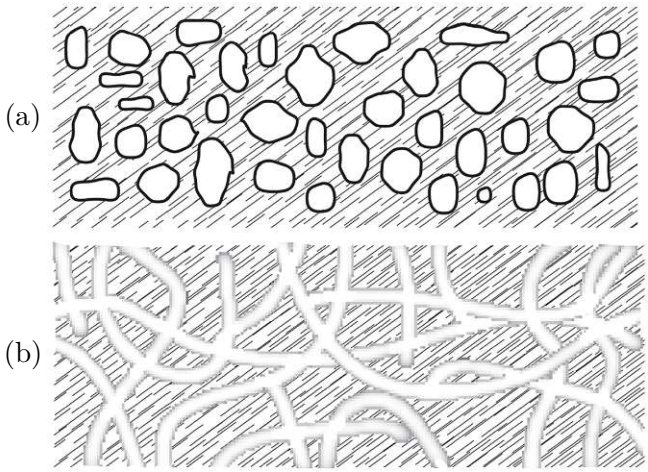

Fig. 3.5. Closed- (a) and open-pore (b) structure of porous material, adapted from [41].

impinging acoustic plane wave then simplifies from (3.6) to (3.7):

$$z_\mathrm{s} = -jz_\mathrm{c}\,\cot(kd) \tag{3.7}$$

with z_c and k being the properties of the absorber layer. Although in general the surface impedance and, subsequently, the absorption and reflection coefficient vary with the angle of incidence, (3.7) is a good approximation for many porous materials [41].

To gain an insight on the dependence of the absorption coefficient on the absorber thickness d, porous absorbers of two different thicknesses where measured in a reverberation room [41]. The resulting values for the absorption coefficient are shown in Fig. 3.6, which shows a strong dependence on the acoustic frequency. Low frequencies are difficult to attenuate using only porous absorbers. On the other hand, high frequencies can be reduced quite effectively using porous absorbers.

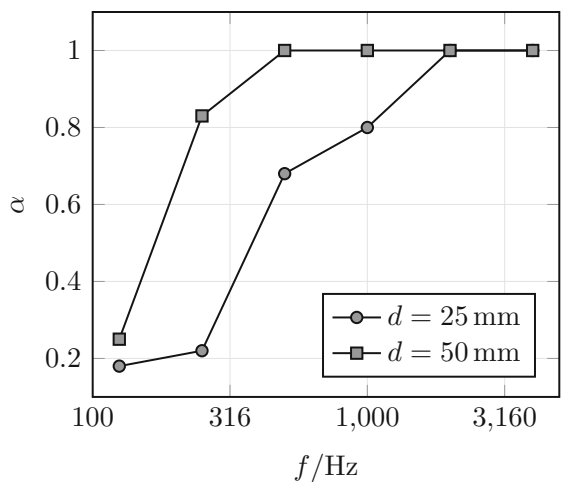

Fig. 3.6. Absorption coefficient in dependence of the frequency for foams of different thicknesses, adapted from [41].

3.2.1 Porous materials

The three main porous material types which have proven to effectively absorb sound are foams, fibrous materials, and granular materials. In the following, only foams and fibrous material types will be outlined with special attention paid to their importance for aero-engine liners, as **granular materials** are insignificant for aero-engine liners.

Foams can be manufactured as open or closed structures as depicted earlier in Fig. 3.5. The highest absorption levels can be achieved with high reticulation and open pore structures, as the acoustic waves can travel mainly in the flow medium between the interconnected cells. Closed structure foams can also be manipulated by perforations to gain better absorption characteristics, but will still not be as adequate as open structure foams when it comes to acoustic attenuation. With decreasing reticulation rates, properties such as the flow resistivity and the tortuosity as well as the absorption of low-frequency sound is increased, whereas the perfomance of mid- to high-frequency absorption is reduced [41].

One cheap foam material used for room acoustics is Polyurethane, which does not withstand the harsh conditions inside an aero-engine. Aero-engine liners can be enhanced with metal or ceramic foams, which offer higher material strength properties and fire resistance but also come at a high price due to their expensive manufacturing. There has been recent research on dead-end pores added to metallic foams, which result in the increased absorption of frequencies defined by the length of the dead end pores. Attenuation of lower frequencies was successfully achieved by the periodic selection of the dead-end pores' length [41].

Fibrous materials can be made artificially or harvested from natural resources. Artificial fibrous materials are glass, rock or basalt fibres, which are manufactured by melting the raw materials and spinning or pulling them into woolly filaments. The filaments get their more robust final shape by the use of a binder and form an interconnected network of air passages, which allows acoustic pressure waves to propagate. Anisotropic behaviour of the acoustic properties results in the case of fibre layers with equal orientation of the fibres. In general, fibre dimensions, fibre composition, fibre orientation, and binder properties have an impact on acoustic properties.

3.3 Resonant absorbers

Resonant absorbers function in a different way to the porous absorbers discussed in the previous section. Their working principle is to convert sound energy into kinetic energy by exploiting oscillatory system properties of specially formed cavities. The two main resonator designs are the **Helmholtz** and the **membrane resonator**, whereby the latter will not be treated in greater detail as its significance for aero-engine sound attenuation is negligible. However, Helmholtz resonance is a mechanism used frequently for noise reduction and is known best for the resonance produced by blowing across the top of an empty bottle. A simplified description of the underlying resonance physics is that the compressible medium inside the cavity forms a spring which accelerates a proportion of the medium in the cavity

neck. Thereby, a single degree of freedom (DoF) spring-mass oscillator is formed, which is stimulated by the incoming sound waves [41, 44].

The surface impedance of a resonant absorber can be described mathematically as in (3.8) with r_m being the real resistance term and m_a being the acoustic mass per unit area of the panel.

$$z_\mathrm{s} = r_\mathrm{m} + j\left[\omega m_\mathrm{a} - \rho c \cot\left(kd\right)\right] \tag{3.8}$$

(3.8) is altered from (3.7) by adding the resistance term, which represents the acoustic losses, and the mass reactance term, which represents the vibrating plug of acoustic medium. The resonant frequency $f = \frac{\omega}{2\pi}$ of the resulting single layer resonant absorber can then be determined by setting the imaginary part of (3.8) to 0, which concludes to (3.9):

$$\omega m_\mathrm{a} - \cot\left(\frac{\omega d}{c}\right) = 0 \tag{3.9}$$

(3.9) can be linearized in the case of cavity sizes much smaller than the acoustic wavelength ($kd \ll 1$) so $\cot(kd) \rightarrow \frac{1}{kd}$, which results in (3.10):

$$f = \frac{c}{2\pi}\sqrt{\frac{\rho}{m_\mathrm{a} d}}. \tag{3.10}$$

Depending on the absorber design, low to mid frequency ranges can be affected therewith, which results in a major advantage compared to porous absorbers. On the downside, only a narrow absorption bandwidth is achieved with simple resonant absorbers. Nevertheless, multiple absorber mechanisms can be joined in devices to maximize sound attenuation, as will be outlined later on.

3.3.1 Helmholtz resonance

Helmholtz resonance is a key mechanism in resonant absorption and is used to effectively absorb low frequencies. As the losses of perforated panels with hole diameters larger than the BL established by the acoustic flow are rather small, Helmholtz absorbers often contain porous absorber plates. These porous plates increase the losses when placed close to the perforations, where the particle velocities are high. A Helmholtz absorber with periodic placement of perforations, a porous absorbent and an attached cavity is depicted in Fig. 3.7. To adopt (3.8) to Helmholtz absorbers, the acoustic mass can be calculated using (3.11). The term containing δ, which accounts for the end-correction factor, considers the additional vibrating mass to the hole volume as radiation impedance has to be considered. The last term with η being the dynamic viscosity of the fluid medium considers BL effects, which becomes significant only for holes with submillimetre diameters. The final expression for m_a results in (3.11):

$$m_\mathrm{a} = \frac{\rho}{\epsilon}\left[t + 2\delta a + \sqrt{\frac{8\nu}{\omega}\left(1 + \frac{t}{2a}\right)}\right] \tag{3.11}$$

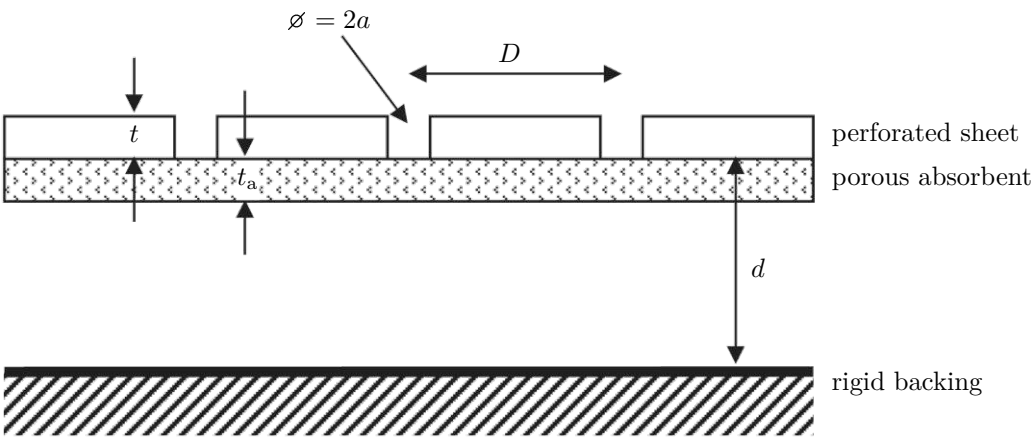

Fig. 3.7. Helmholtz absorber with a porous absorbent, adapted from [41].

with ϵ being the fraction of open area according to (3.12) for cylindrical holes in a square pattern:

$$\epsilon = \frac{\pi a^2}{D^2} \tag{3.12}$$

To model the losses of a simple Helmholtz absorber without porous layers, two expressions have been established through (3.13) and (3.14) with the restriction for (3.13) not to be used for submillimetre perforations:

$$r_\mathrm{m} = \frac{\rho}{\epsilon}\sqrt{8\nu\omega}\left(1 + \frac{t}{2a}\right), \tag{3.13}$$

and

$$r_\mathrm{m} = \frac{\sqrt{2\rho\eta\omega}}{2\epsilon}, \tag{3.14}$$

with ν being the kinematic viscosity of the fluid medium [45]. The values of both expressions and the difference between them is very small for standard Helmholtz resonators, which require additional porous absorbent layers to increase absorption levels.

3.3.2 Microperforated panel absorbers

When decreasing the perforation diameter to submillimetre sizes, the BL in the holes increases viscous losses significantly and cancels out the need for porous absorbent layers. To model the acoustic behaviour of such microperforated panels (MPP), the sound propagation in a single tube that is short compared to the wavelength, was used to derive the tube's specific acoustic impedance in (3.15) by the use of the first kind Bessel function of zero (J_0) and first order (J_1):

$$z_1 = j\omega\rho t\left(1 - \frac{2J_1\left(k'\sqrt{-j}\right)}{k'\sqrt{-j}J_0\left(k'\sqrt{-j}\right)}\right)^{-1} \tag{3.15}$$

with

$$k' = a\sqrt{\frac{\rho\omega}{\eta}}. \tag{3.16}$$

There are approximated formulas for (3.15), but with today's numerical solutions the expression can be implemented directly to avoid approximation errors [41, 46]. A microperforated panel absorber (MPA) consists of an **MPP**, a **cavity** and a **rigid backing** as shown in Fig. 3.7 without the porous layer. To obtain the surface impedance for an MPA, the cavity impedance $-j\rho c \cot(kd)$ and the losses according to (3.14), as well as a term for the end correction, have to be considered, which finally results in (3.17):

$$z_{\mathrm{h}} = \left[\frac{z_1}{\epsilon} - j\rho c \cot(kd) + \frac{\sqrt{2\omega\rho\eta}}{2\epsilon} + \frac{j1.7\omega\rho a}{\epsilon} \right] \cos(\psi). \tag{3.17}$$

(3.17) describes the surface impedance for an oblique incident angle ψ and contains the analytic solution of z_1 from (3.15). It has to be noted that non-linear effects have to be taken into account for high acoustic intensities or grazing flow velocities [47].

There has been researched dividing the cavity into smaller segments, as oblique incidence minders the absorption capabilities of Helmholtz absorbers, with non-partitioned backing cavity and without implemented porous plates. Hexagonal partitions have been proven to not only enhance acoustic absorption, but also the structural strength of the absorber devices [41, 48].

One advantage of MPAs over porous absorbents is that the microperforations tend to clog up less during service due to the vibrating plug of fluid medium inside the perforations. Moreover, MPAs qualify as lightweight assemblies, as it has been shown that the best absorption rate can be achieved by designing the panel thickness t equal to the perforation diameter $2a$ [41, 46]. As the acoustic properties are independent of the material used for the MPP, metal or other high-strength materials such as carbon fibre reinforced polymer (CFRP) can be used to further reduce the device's weight. Generally, the MPA's importance as an acoustic treatment has been increasing over recent years, which has been enabled through a broad application field [41, 49].

3.4 Aero-engine application

Aero-engine liners can be applied to the cylindrical boundaries of the engine's inner geometry. By placing the absorber devices on as much duct wall area as possible, acoustic attenuation can increase. Fig. 3.8 shows the consequences of extensive liner application to the inner duct surfaces of a turbofan engine. It can be seen that the noise propagating from the rotor and rotor-stator sources through the bypass section to the exhaust section is reflected very often and as a result, those acoustic modes will be attenuated more than the modes propagating towards the engine's inlet section [4].

In order to maximize the area that acoustic liners can be applied to in the case of ducted flows, their robustness has been increased. Thereby, so-called splices can be avoided, which are non-lined spaces in the circular direction of the duct walls that ensure required material strength [50]. There has also been research on acoustic liner application for subsonic ducted fans,

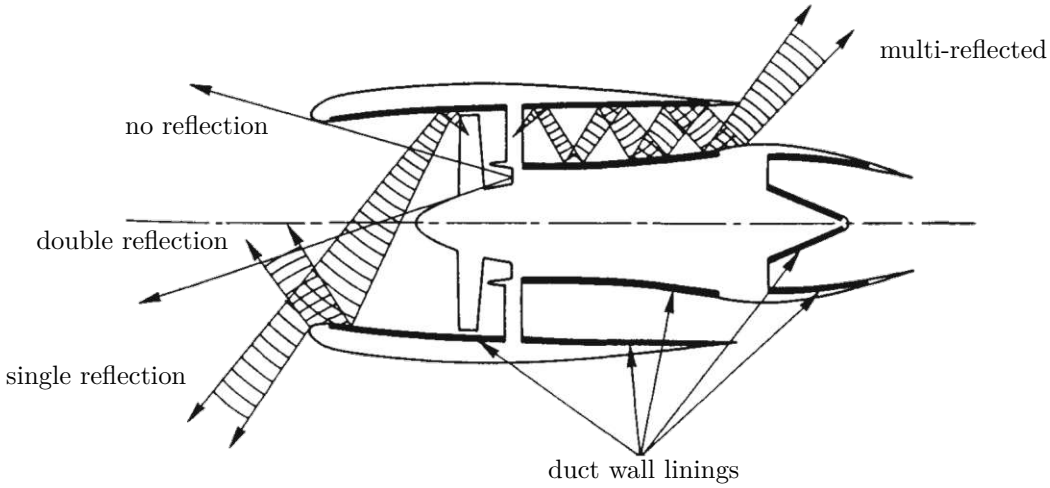

Fig. 3.8. Reflection paths inside a turbofan, adapted from [4].

where absorber linings were placed directly in the rotor plane, which resulted in significant reduction in the fan's aerodynamic efficiency [51].

3.4.1 Linear/Perforate liner

Liner design in modern aero-engines varies mainly with the facesheet designed and the cavity depth chosen. Fig. 3.9 shows the two main aero-engine liner configurations used nowadays [4]. The so-called **linear liner** in Fig. 3.9a consists of a woven facesheet, a cavity which is hexagonally partitioned and a rigid backing. Facesheets made from aluminium or stainless steel wire cloth show good absorption bandwidth and are able to withstand a wide range of environmental conditions. In Fig. 3.9b, a **perforate liner** with a perforated facesheet is presented. Its set-up is identical to the linear liner, apart from the facesheet, which can be made from aluminium, titanium or CFRP [4, 50].

One challenge in manufacturing aero-engine liners it to permanently join the hexagonal

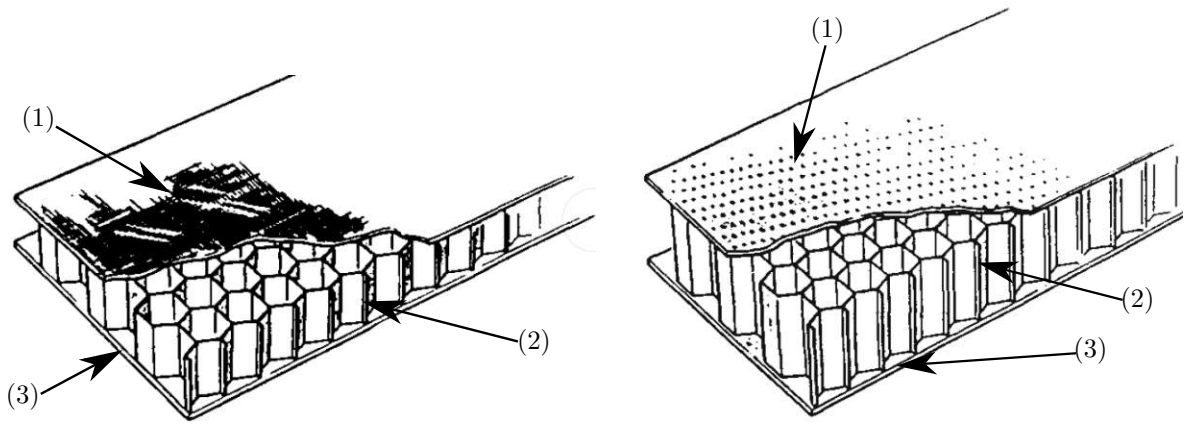

(a) Linear liner **(b)** Perforate liner

Fig. 3.9. Comparison of linear and perforate liner with facesheet (1), honeycomb structure (2) and rigid backing plates (3), adapted from [4].

partitioning structure to the absorbing panel without blocking a fraction of the absorber panel's area. The blockage of the facesheet must be minimised to maximize noise attenuation [4]. A further increase in the acoustic dissipation can be achieved by using a flexible material with damping properties such as a honeycomb support structure [44].

3.4.2 Multiple DoF liner

Widening the absorption bandwidth of an aero-engine liner can be important to account for the different operating conditions, that result in different noise frequencies. One possibility is to use multiple degree of freedom (DoF) liners, which are able to combine multiple resonant absorbers of multiple resonance frequencies and porous absorbers in liner device. Even though such devices are difficult to manufacture, bigger in size and more expensive, they are widely used to attenuate aero-engine noise [4, 41, 50]

Fig. 3.10 shows a double Dof perforate liner with two different cavity depths to effectively suppress a wider bandwidth of frequencies. The rigid backing and partitioning support structures have to fulfil identical requirements as those of the single DoF liners from Fig. 3.9. The so-called septum, which stands for the intermediate panel layers, can be designed as perforated or linear sheet.

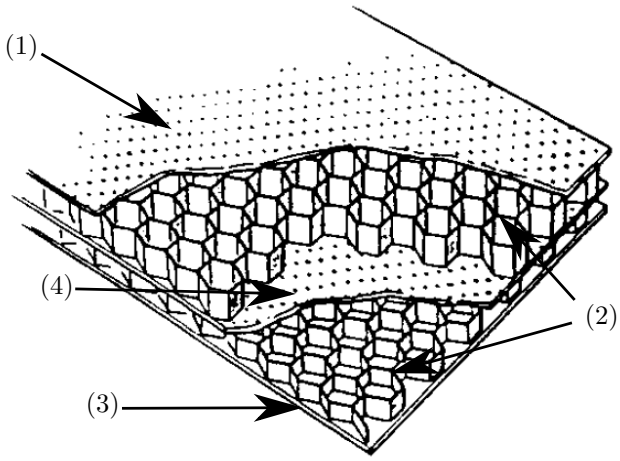

Fig. 3.10. Double DoF linera with a facesheets (1), honeycomb structures (2), rigid backing plate (3) and septum (4), adapted from [4].

Chapter 4

Acoustic measurement

4.1 Methodology

In Chap. 4.1, the measuring process is explained by documenting the measuring task itself and the methods applied to accomplish this. The EDF unit considered with the ID-number 01-7200-M is composed as shown in Fig. 2.1 and its characteristic properties, as well as its inner dimensions, are listed in Tab. 4.1. The EDF unit to be measured acoustically, is mounted inside a propulsion test stand (PTS) made of an aluminium-beam construction, which has to be considered in the measuring problem as external noise, especially because of its installed power supply unit.

Tab. 4.1. Characteristic properties and dimensions of EDF unit 01-7200-M.

component	diameter	axial length	no. of blades
duct	201.3 mm	250 mm	-
stator	-	50 mm	4
rotor	200 mm	27 mm	7

Two main goals are pursued by the measurements done during the initial testing campaign (ITC). Firstly, the EDF's acoustic emissions, regarding sound power and pressure levels, are to be characterised at an operating range of between 6000 min^{-1} and 12 000 min^{-1}. Four operating points are defined for closer examination, which are characterised by the value of the rotor's rotational speed. Those operating points with the corresponding BTS and BPF are listed in Tab. 4.2. As can be seen clearly, the BTS values are all subsonic, and the main

Tab. 4.2. Characteristic values of EDF unit 01-7200-Mat different operating points.

operating point	rotational speed	BTS	f_{BPF}	f_{LF}
OP 1	6000 min^{-1}	62 m/s	700 Hz	1400 Hz
OP 2	8000 min^{-1}	83 m/s	933 Hz	1866 Hz
OP 3	10 000 min^{-1}	104 m/s	1167 Hz	2343 Hz
OP 4	12 000 min^{-1}	125 m/s	1400 Hz	2800 Hz

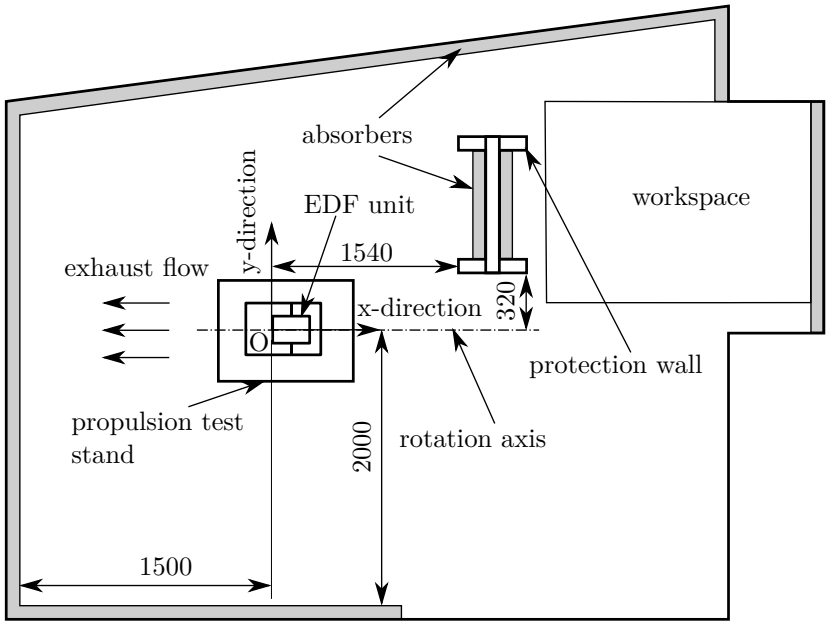

Fig. 4.1. Positioning of the propulsion test stand inside the measuring room.

frequency of the ECM's electromagnetic local forces matches the second harmonic of the BPF, as the number of ECM poles $p = 14 = 2B$.

The second goal of the EDF measurements is to provide sufficient information about the EDF unit's acoustic field at the main operating point OP 4 to allow the dimensioning of the appropriate MPA. Additionally, indicators have to be determined which allow an evaluation of the change of the EDF's acoustic emissions when the MPAs are laid out and installed.

4.1.1 Measuring set-up

The Institute's low-reflection room has been used as the location for conducting the necessary measurements, due to its sound absorbing properties. Inside the low-reflection room, the PTS was positioned at a centred position, so that the airflow was able to circulate with the lowest disturbances possible. As can be seen in Fig. 4.1, the PTS was positioned accordingly to place the EDF's rotation axis at an equal distance from each side wall. The setup presented, allowed the EDF's exhaust flow, to travel unhindered for more than 1 m. In addition to the measuring object, a mobile protection wall needed to be put up, to ensure safety for the people present in the measuring room during the EDF unit's operation. The porous absorber panels used in the measuring room and on the protection wall is *Basoplan 100*, which results in the room's frequency dependent reverberation time as shown in Fig. 4.2a [52].

4.1.2 Enveloping surface method

The most important acoustic indicator to determine a machine's acoustic emissions is the acoustic power level [22]. In [22], the enveloping surface method (ESM) is mentioned as a possible measuring method to determine the sound power level of an acoustic source using an anechoic measuring room. The international standard DIN EN ISO 3745 contains all the

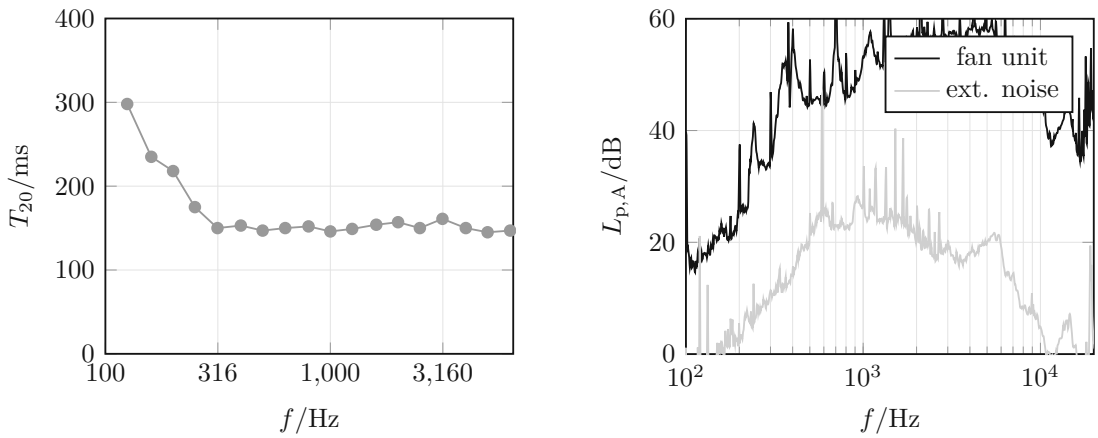

(a) Reverberation time.

(b) External noise.

Fig. 4.2. Measuring environment's reverberation time and external noise.

necessary information and procedures to conduct the measurements needed for accuracy class 1. As the claims to the anechoic room have to be proven according to ISO 26101 and are very restrictive, measurements for accuracy class 1 cannot be taken without unreasonable effort. However, a measuring method with the lower accuracy class 2 is described in the international standard DIN EN ISO 3744 and can be conducted with fewer resources [53–55].

The criteria of the external noise's SPL have to be fulfilled relative to the measuring object's SPL in order to use the methods in [53]. Therefore, in Fig. 4.2b, the measurement data of the external noise was plotted against the measurement of the EDF unit at its quietest operating point OP1. Due to rather high acoustic pressure levels of the measuring object, the criteria of 6 dB difference and even the recommendation of 15 dB between external noise and the measured sound is met at all narrowbands, except for the bands at 125 Hz and 600 Hz.

A half sphere with the radius of 1 m was used as a measuring surface for the enveloping surface method and its coordinate origin was placed at the outlet centre of the cylindrical duct projected on the floor underneath, according to Fig. 4.1. The $N_{\mathrm{M}} = 10$ microphone

Tab. 4.3. Cartesian coordinates of the microphone positions for the ESM measurements.

Number of microphone position	x-direction	y-direction	z-direction
1	160 mm	−960 mm	220 mm
2	780 mm	−600 mm	200 mm
3	780 mm	550 mm	310 mm
4	160 mm	900 mm	410 mm
5	−830 mm	320 mm	450 mm
6	−830 mm	−400 mm	380 mm
7	−260 mm	−650 mm	710 mm
8	740 mm	−70 mm	670 mm
9	−260 mm	500 mm	830 mm
10	100 mm	−100 mm	990 mm

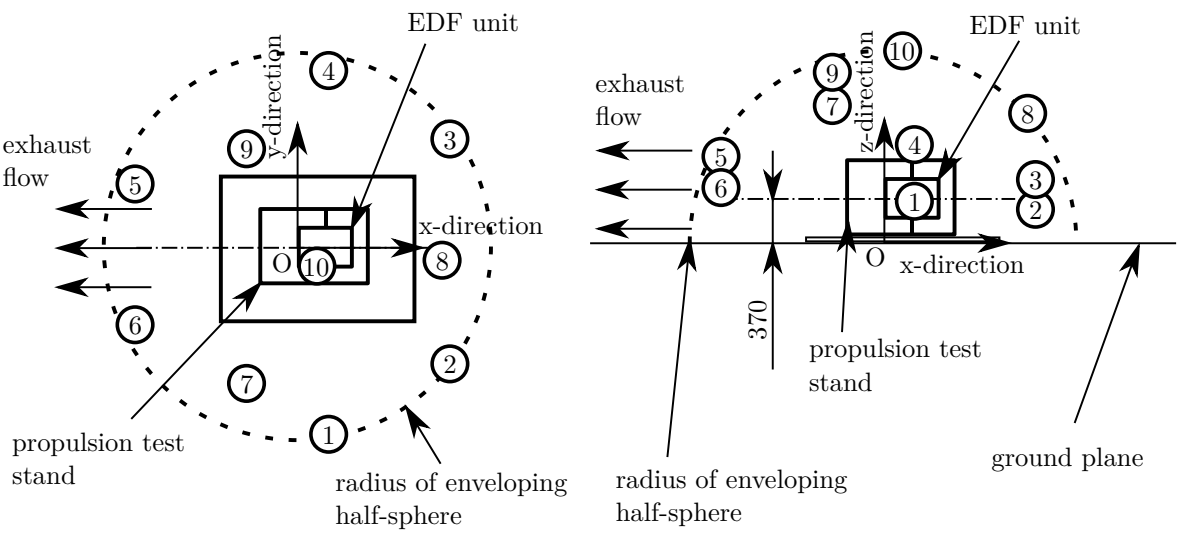

(a) Visualisation in the xy-plane. **(b)** Visualisation in the xz-plane.

Fig. 4.3. Visualisation of the microphone positions for the ESM measurements relative to the PTS.

positions for general sound sources, according to [53], are then given by the cartesian values in Tab. 4.3. As can be seen in Fig. 4.3b, the PTS has to be positioned on the floor to meet the requirement of the reflective surface as the wooden baseplate has a low absorption coefficient across the audible frequency bandwidth [56]. To conduct the ESM, measurements of both the measuring object's and the external noise's acoustic emissions have to be taken. By doing so, the external noise's contribution to the sound power level of the measuring object can be eliminated. Therefore, the time-averaged frequency-band, sound pressure levels $L'_{pi(\mathrm{ST})}$ of the measuring object and external noise $L_{pi(\mathrm{B})}$ at each microphone position are filtered out of the respective measurement data to determine their mean values over the measuring surface $\overline{L'_{p(\mathrm{ST})}}$ for the measuring object in (4.1):

$$\overline{L'_{p(\mathrm{ST})}} = 10\lg\left[\frac{1}{N_\mathrm{M}}\sum_{i=1}^{N_\mathrm{M}} 10^{0.1L'_{pi(\mathrm{ST})}}\right]\mathrm{dB} \tag{4.1}$$

and $\overline{L_{p(\mathrm{B})}}$ for the external noise in 4.2:

$$\overline{L_{p(\mathrm{B})}} = 10\lg\left[\frac{1}{N_\mathrm{M}}\sum_{i=1}^{N_\mathrm{M}} 10^{0.1L_{pi(\mathrm{B})}}\right]\mathrm{dB}. \tag{4.2}$$

Subsequently, the external noise correction factor K_1 can be calculated by 4.3:

$$K_1 = -10\lg\left(1 - 10^{-0.1\Delta L_p}\right)\mathrm{dB} \tag{4.3}$$

where the sound pressure level difference ΔL_p between the measurement object's and the external noise's time- and space-averaged, frequency-band, sound pressure levels is determined in 4.4:

$$\Delta L_p = \overline{L'_{p(\mathrm{ST})}} - \overline{L_{p(\mathrm{B})}} \tag{4.4}$$

In order to consider the measuring room's reflections, the correction factor K_2 has to be computed according to (4.5), where S is the area of the enveloping measuring surface.

$$K_2 = 10\,\lg\left[1 + 4\frac{S}{A}\right]\,\mathrm{dB} \tag{4.5}$$

The equivalent sound absorption area A of the measuring room has to be computed by the Sabine formula (4.6) using the data from the reverberation time measurements after DIN EN ISO 3382-2 [57].

$$A = 0.16\frac{V}{T_\mathrm{n}} \tag{4.6}$$

In (4.6), V is the measuring room's volume and T_n is the reverberation time for a 60 dB drop of the sound pressure level in a frequency band after turning off the acoustic source. Knowing both correction factors K_1 and K_2, the time-averaged frequency-band sound pressure level $\overline{L_\mathrm{p}}$ on the measuring surface can be computed by 4.7:

$$\overline{L_p} = \overline{L'_{p(\mathrm{ST})}} - K_1 - K_2 \tag{4.7}$$

which furthermore allows the final calculation of the measuring object's sound power level $\overline{L_\mathrm{W}}$ using the relation 4.8 between $\overline{L_\mathrm{p}}$, S and $S_0 = 1\,\mathrm{m}$.

$$\overline{L_W} = \overline{L_p} + 10\,\lg\frac{S}{S_0}\mathrm{dB} \tag{4.8}$$

In order to gain the maximum of information of the measuring results, the sound power levels ought to be computed for narrow frequency bands, octave and third octave frequency bands, as well as for the A-weighted frequency bands.

4.1.3 Microphone array measuring

A closer examination of the acoustic sources of the measuring object is provided by using a microphone array. Multiple microphones positioned at fixed locations provide synchronized measuring data, which can be used to spatially determine acoustic sources by applying different *beamforming* algorithms to the measured data [22].

The microphone array provided by the Institute is a two-dimensional spiral array with 63 electret microphones. For the measuring of rotating sound sources, only the $N = 32$ microphones positioned on a ring with radius $\varrho_\mathrm{x} = 0.42\,\mathrm{m}$ were needed. A MATLAB implementation of a *beamforming* algorithm for rotating sound sources was already developed in [58].

The sound mechanisms of the highest importance in the case of subsonic ducted fans operate on the fan blades and stator vanes. Therefore, installing the microphone array at a coaxial position to the fan's rotational axis enabled it to measure the unreflected acoustic waves directly from the rotor front. Measurement from the negative x-direction would expose the microphones to high velocity fluctuations for which reason measurements were taken from the positive x-direction with the microphone array facing the inlet section of the EDF unit.

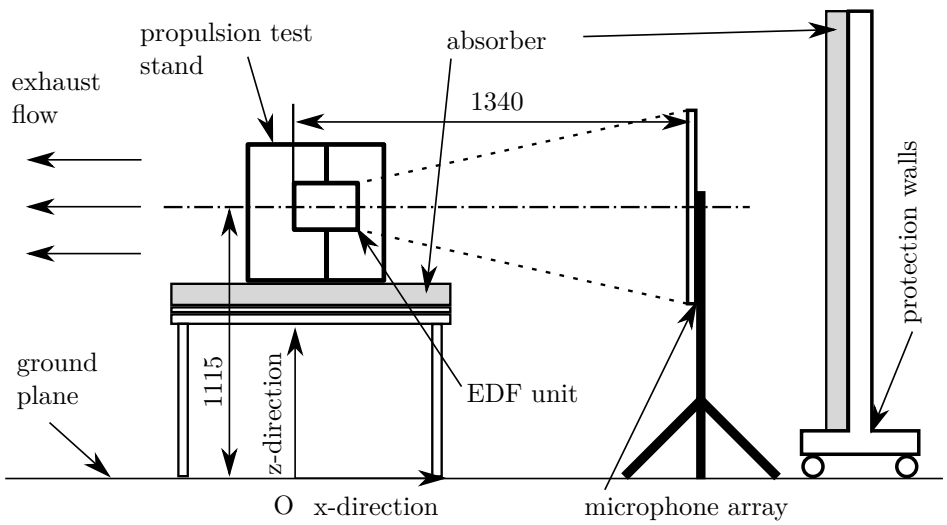

Fig. 4.4. Positioning of the microphone array relative to the PTS for measuring.

The chosen setup for the microphone array measurements is depicted in Fig. 4.4. As can be seen, the PTS was installed on a table with a porous absorber plate directly underneath to minimize reflections from the table-top. The distance between the microphones and the front rotor plane was 1.15 m To check the EDF's working conditions against the microphone array's measuring capabilities, three estimations of limiting frequencies were done hereafter. The highest sound frequency $f_{\max}$ that can be measured without spatial aliasing due to the discrete microphone positions is calculated in (4.9):

$$f_{\max 1} = \frac{c}{2\Delta x} = \frac{c}{4\varrho_{\mathrm{x}} \sin\left(\frac{\pi}{N}\right)} = 2083\,\mathrm{Hz} \tag{4.9}$$

where Δx is the distance between two neighbouring microphones. As calculated in (4.9) for the setup used, spatial aliasing potentially occurs for frequencies higher than 2083 Hz.

As second condition for the measuring capabilities, which also accounts for the sound sources' speed, (4.10) is mentioned in [58].

$$f_{\max 2} = \frac{N \cdot (c - \Omega\,\varrho_{\mathrm{y}})}{4\,\pi\,\varrho_{\mathrm{y}}} \tag{4.10}$$

However, when calculating $f_{\max 2}$ for the critical operation point OP4 and the critical source radius $\varrho_{\mathrm{y}} = 0.1\,\mathrm{m}$, (4.10) results in $f_{\max 2} = 5534\,\mathrm{Hz}$.

Microphone array measurements are also restricted towards lower frequencies through the sparrow limit r_{sl}, which represents the minimum distance between two points of equal strength that can be separately resolved by a microphone array's measurements [14, 59]. The Sparrow limit is calculated in (4.11):

$$r_{\mathrm{sl}} = 0.47 \frac{\lambda}{\sin\theta_{\mathrm{a}}} \tag{4.11}$$

with λ being the acoustic wavelength, and θ_{a} being the aperture half angle of the array's microphones to a source point. Considering a point on the fan's rotational axis located on

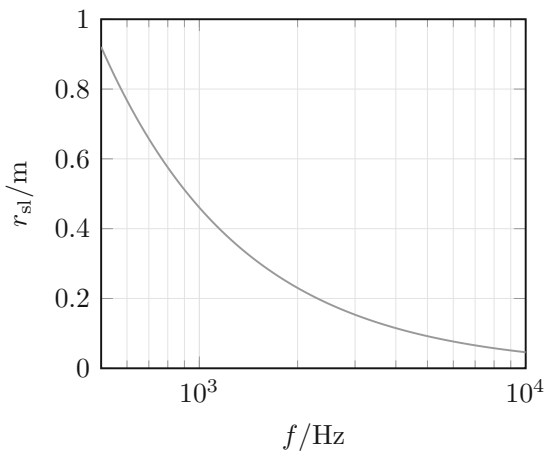

Fig. 4.5. Sparrow limit of the microphone array setup used.

the front rotor plane, $\theta_a = 20.5°$ Plotting r_{sl} in dependence on the acoustic frequency f for the used microphone array setup in Fig. 4.5 reveals the resolution for low frequency sources of the used setup. Due to the small fan diameter of 0.2 m, the microphone array results will only become meaningful for frequencies higher than $f_{min} = 3\,\text{kHz}$.

4.2 Measuring results

In the current Chapter, the results for the acoustic measuring of the unmodified fan unit are presented and discussed. A measuring time of $t_m = 20\,\text{s}$ was chosen for the measurements at constant rotational speed. The sampling rate for all acoustic measurements was $f_s = 48\,\text{kHz}$, which, according to the Nyquist-Shannon theorem, allows the detection of frequencies of up to $f_{max} = 24\,\text{kHz}$ without temporal aliasing. Further, the SPL presented are A-weighted to allow a focused comparison of the data measured with the data of the modified fan in the subsequent Chapter in regard of the differences to human perception.

In Fig. 4.6a and Fig. 4.6b, the measurement setup for the ESM and the microphone array measurements are shown respectively

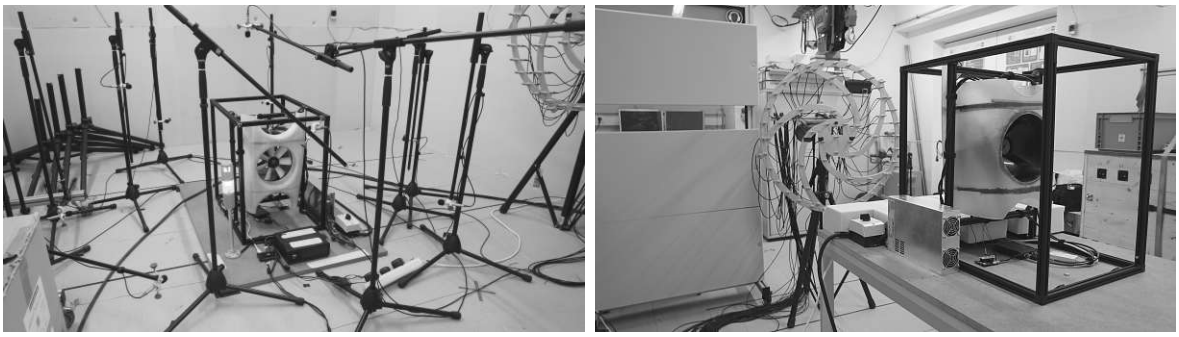

(a) ESM setup. **(b)** Microphone array setup.

Fig. 4.6. Pictures of the two measuring methods in the Institutes measuring room.

4.2.1 Far-field radiation

As explained in Chap. 4.1, the total sound pressure and sound power levels emitted were measured according to [53]. An important acoustic property of ducted fans, as pointed out in Chap. 2, is the directivity pattern of acoustic pressure waves that exit either the duct's inlet or outlet.

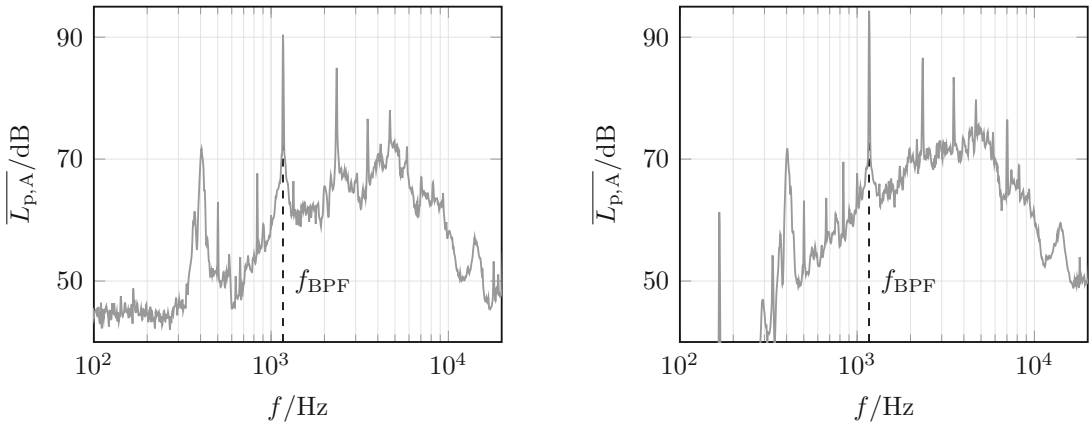

(a) Microphone position 5 **(b)** Microphone position 8

Fig. 4.7. Narrowband $\overline{L}_{\mathrm{p,A}}$ at microphone positions 5 and 8 of EDF at OP3.

In Fig. 4.7, the narrow band SPL of the EDF at OP3 measured at two discrete microphone positions are shown. Fig. 4.7a shows the measurement results at the outlet microphone position 5, whereas Fig. 4.7b shows the results at microphone position 8, which is located close to the fan inlet. The main sound frequencies at both measurement locations are the BPF and its higher harmonics, which leads to the rotor and motor, as well as to the rotor-stator interactions, as being the main sound sources at this OP. Nevertheless, a clear difference between the SPL in Fig. 4.7a and Fig. 4.7b can be identified. The general amplitude difference at the observed microphone positions, on the one hand, depends on the different distances between the measuring positions to the rotor source mechanism and, on the other hand, on the different duct lengths the rotor sound has to propagate through. As shown in Chap. 2, rotor sound pressure waves decay exponentially over the distance in a circular duct for subsonic fans. The smaller peaks in amplitude at the multiples of N, which surround the BPF and its harmonics can be explained by the spinning modes excited through rotor-stator interactions, which were treated in Chap. 2. Additionally, those tonal noise emissions can also be generated by mechanisms in the electric motor, which will be shown in Chap. 5.2.2. In theory, the rotor-stator spinning modes are more likely to surpass the amplitudes of rotor spinning modes in subsonic ducted fans, yet the measurements show the opposite behaviour for the harmonics of the rotational speed. One reason is the design intents that were already considered in the current fan design to minimise rotor-stator interactions by increasing the distance between the stator and the rotor plane and by introducing a sweep angle to the stator vanes. Additionally, the duct length of the considered EDF unit is rather short, especially in the inlet section.

The difference in the broadband SPL is also dominant. At frequencies below 400 Hz, the outlet microphone position shows significantly higher SPL, which can be assigned to the exhaust flow velocities. The broadband SPL of higher frequencies can be again explained by the shorter distance from the source mechanisms to microphone 8. The narrowband SPLs at different operating points are illustrated in Fig. 4.8. It can be seen that at all the operating points considered, at least the four highest tonal amplitude peaks are all the BPF or its higher harmonics. At OP1, the highest amplitude is the third harmonic frequency at $f = 2100\,\mathrm{kHz}$, whereas the BPF itself becomes the highest amplitude at the other operating points with higher rotational speed.

The broadband SPL over the whole spectrum considered continuously increases with the increasing rotational speed, which can be explained by the higher intensities of the turbulent source mechanisms due to higher flow velocities. The only constant tonal peaks over all the operating points are two peaks at above 15 kHz, which represent the frequency of the electronic speed controller's pulse width modulation (PWM) signal for the electronic commutation. Two narrowband SPL peaks that are of interesting behaviour, are at 350 Hz

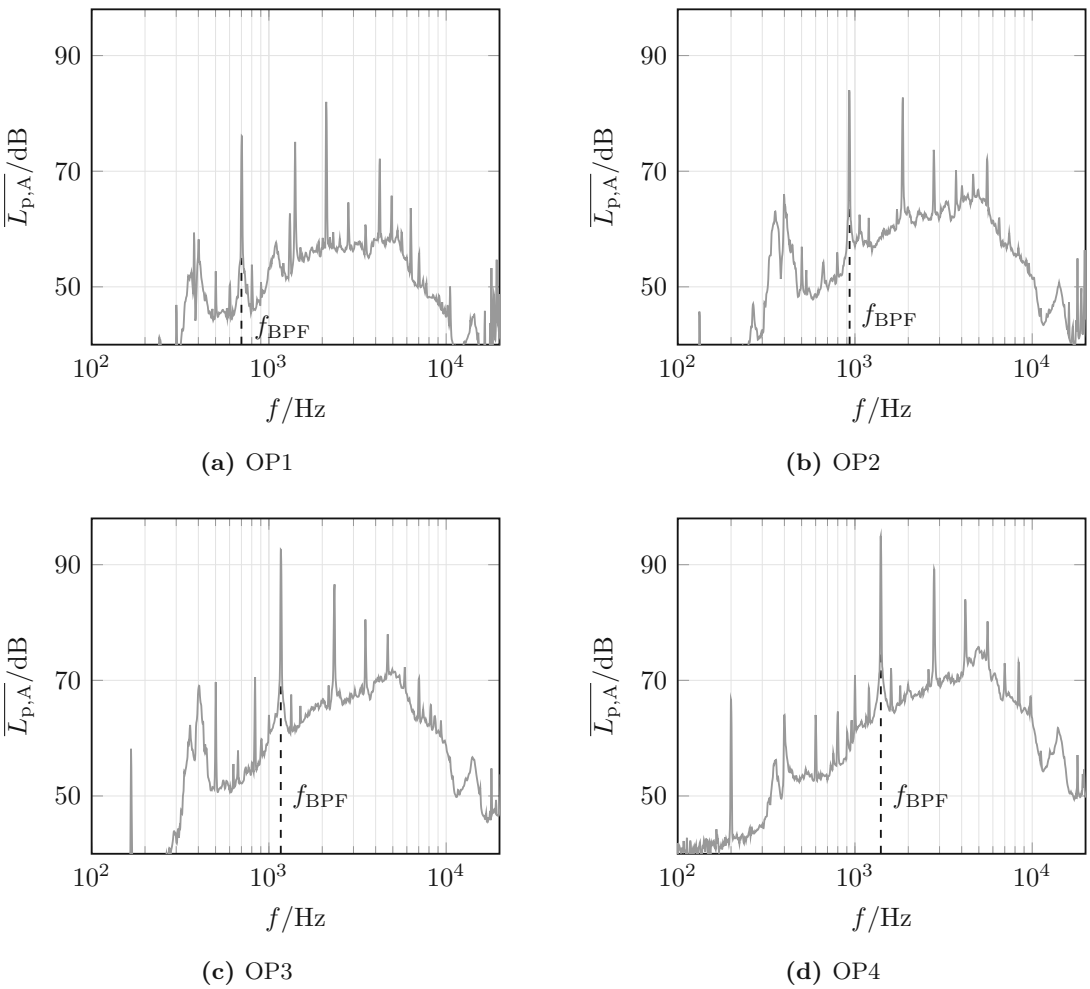

Fig. 4.8. Narrowband $\overline{L_{\mathrm{p,A}}}$ at different operating points.

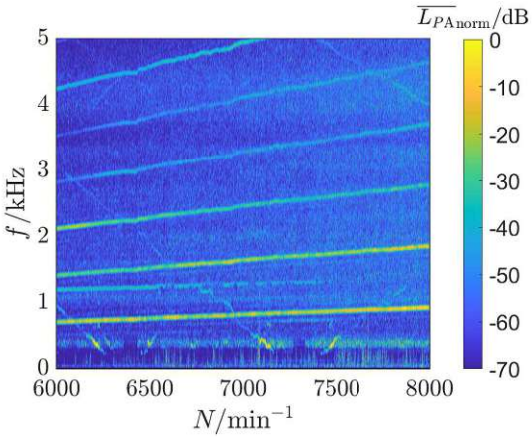

(a) Spectrogram between OP1 and OP2

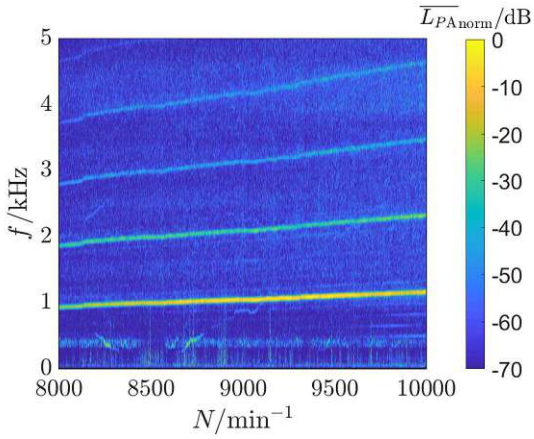

(b) Spectrogram between OP2 and OP3

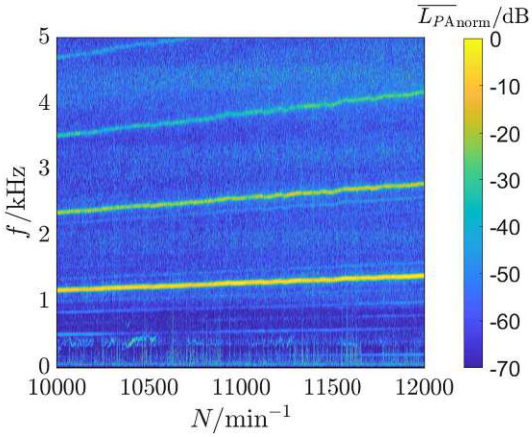

(c) Spectrogram between OP3 and OP4

Fig. 4.9. Spectrograms of the fan unit in its operating range.

and 400 Hz. Their frequency range appears constant over the observed operating points, whereas the amplitude varies with the rotational speed in a non-linear way.

Additional measurements that were performed with the microphone configuration of the ESM are transient measurements with a constant ascend of the rotational speed. Therefore, 40 s measurements were done between each neighbouring operating point. A time gradient of $50\,\mathrm{s}^{-2}$ results due to the difference in rotational speed of $2000\,\mathrm{min}^{-1}$ between the operating points. The spectrograms in Fig. 4.9 are calculated by the *MATLAB* function *spectrogram()* and the SPL $\overline{L_{PA\text{norm}}}$ denotes the measured SPL relative to the highest SPL in the respective spectrogram. Again, the BPF and its harmonics are confirmed to represent a significant contribution to the noise level emitted. The m-lobed spinning patterns from the rotor-stator interaction are represented by the constant lines dividing the BPF and its harmonics and can be distinguished clearly in Fig. 4.9b and Fig. 4.9c. In Fig. 4.9a at $6500\,\mathrm{min}^{-1}$ and in Fig. 4.9b at $8100\,\mathrm{min}^{-1}$, as kinks in the BPF and the harmonics are present, which increase in the higher harmonic frequencies. This phenomenon can be traced back to small deviations in the fan's rotational speed from the ideal speed curve.

In the range between 350 Hz and 400 Hz in Fig. 4.9, the narrowband SPL as determined in

Fig. 4.8 can also be detected and confirmed to have a constant frequency range across the operating range observed. Moreover, the relative difference in amplitude between those narrowband SPLs and the highest amplitude decreases with increasing rotational speed above 9000 min^{-1}. One single tonal component in Fig. 4.9a obtains a constant frequency of around 1200 Hz and decays with increasing rotational speed, while completely vanishing at 7500 min^{-1}.

Repeating artefacts across the speed range from OP1 to OP3 that are linked to the fan's rotational speed can be identified in Fig. 4.9a and Fig. 4.9b as linearly decreasing in frequency, vanishing, and then linearly increasing in frequency with ascending rotational speed. Four of those artefacts can be distinguished across the considered operating range, with the first artefact vanishing between 6300 min^{-1} and 6500 min^{-1}, the second artefact vanishing between 7300 min^{-1} and 7500 min^{-1}, the third artefact vanishing between 8400 min^{-1} and 8600 min^{-1} and the fourth artefact vanishing between 10 200 min^{-1} and 10 400 min^{-1}. For further examination of these artefacts, the electric powertrain was measured solely without the aerodynamic rotor attached in Chap. 5.2.2.

From the transient measurements, the A-weighted overall sound pressure levels (OSPL) were determined for every 6 s, which includes a variation of 300 min^{-1} in the rotational speed. The results, therefore, do not meet the requirements of the DIN EN ISO 3744, with regard to the measuring duration and the stationary process, but nevertheless can be used to make out differences between two configurations when using identical measuring conditions. For that reason, the results of two measurements are shown in Fig. 4.10 to prove the method's reproducibility. By comparing the postprocessed results of the two measurements in Fig. 4.10, the difference between both measurement series can be found to be less than 1 dB over the whole operating range. The measuring object's A-weighted OSPL shows an ascending behaviour with increasing rotational speed of the fan. Two local maxima can be detected in the A-weighted OSPL at around 6500 min^{-1} and 7300 min^{-1}. Those local maxima can be confirmed by taking a closer look at the spectrograms in Fig. 4.9a and Fig. 4.9b. The amplitude at the BPF has a local maximum at those operating points therein, which yields

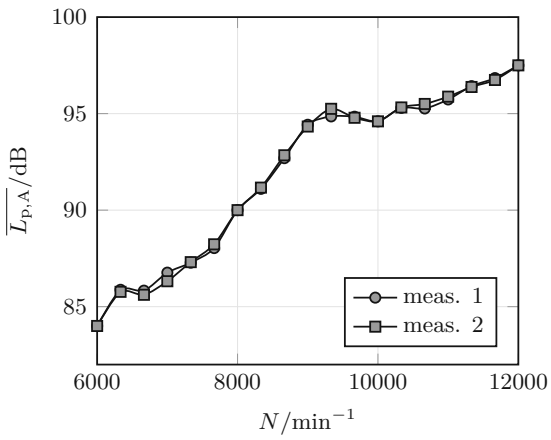

Fig. 4.10. A-weighted OSPL of unmodified EDF unit over operating range.

an explanation for the local maxima in the OSPL.

4.2.2 In-duct sources

As processing algorithm, standard *beamforming* in the frequency domain with a compensation for rotating sources was applied to the measurement data . The square mesh used to calculate the *beamforming* results was chosen to be located on the front rotor plane, with the distance $\Delta x_3 = 1.15\,\mathrm{m}$ to the microphones. With the x_3-coordinate axis being coaxial with the fan's rotational axis, the x_1 and x_2 ranges of the mesh were chosen to be $[-0.11\,\mathrm{m}, 0.11\,\mathrm{m}]$ with a spatial descretization step of 0.5 mm. As the fan's angular position is not measured directly, the acoustic sources cannot be spatially determined relatively towards the fan blade's airfoil profile depth. Nevertheless, conclusions can be drawn on the source's radial position. As described in Chap. 4.1.3, the measurement capabilities of microphone arrays and the setup used are limited to certain frequency ranges. Selected beamforming results of the microphone array measurements at the considered operating points OP1 to OP4 are presented in Fig. 4.11, where each plot additionally contains a circle for the outer dimension of the fan blades. The SPL $L_{p,\mathrm{norm}}$ denotes the measured SPL relative to the highest SPL in the respective sound map.

In Fig. 4.11a, the beamforming result at OP3 performed for the third octave band with centre frequency $f_\mathrm{c} = 0.8\,\mathrm{kHz}$ is shown. As expected from (4.11), the sources at those frequencies cannot be distinguished from each other, and therefore, the location of the source mechanisms at this frequency range can only be said to lie inside the duct's boundaries. Fig. 4.11b shows a beamforming result for the same operating point at the higher third octave band with center frequency $f_\mathrm{c} = 8\,\mathrm{kHz}$. The results show smaller source dimensions, but the possible spatial aliasing prohibits valid statements from being made.

Fig. 4.11c to Fig. 4.11f show the beamforming results for the third octave band with $f_\mathrm{c} = 4\,\mathrm{kHz}$, which represents the fan's third octave band with the highest broadband SPL at each of the considered operating points, as concluded in Chap. 4.2.1. Across the measured operating points, the source locations are calculated to be in the outer radii of the fan. The reason for the broadband sound sources with higher intensity being in the outer radii can be the higher airflow velocities, the blade cross sections are flown around, compared to the inner radii. For OP2, OP3 and OP4, the broadband sound sources are calculated to be at the duct walls, which leads to the sound mechanism being the blade tip vortices.

To allow a more exact localisation or a localisation of sources at lower frequencies, the sparrow limit of the microphone setup has to be decreased by either positioning the microphone array closer to the duct inlet, or using a microphone array with a larger radius ϱ_x.

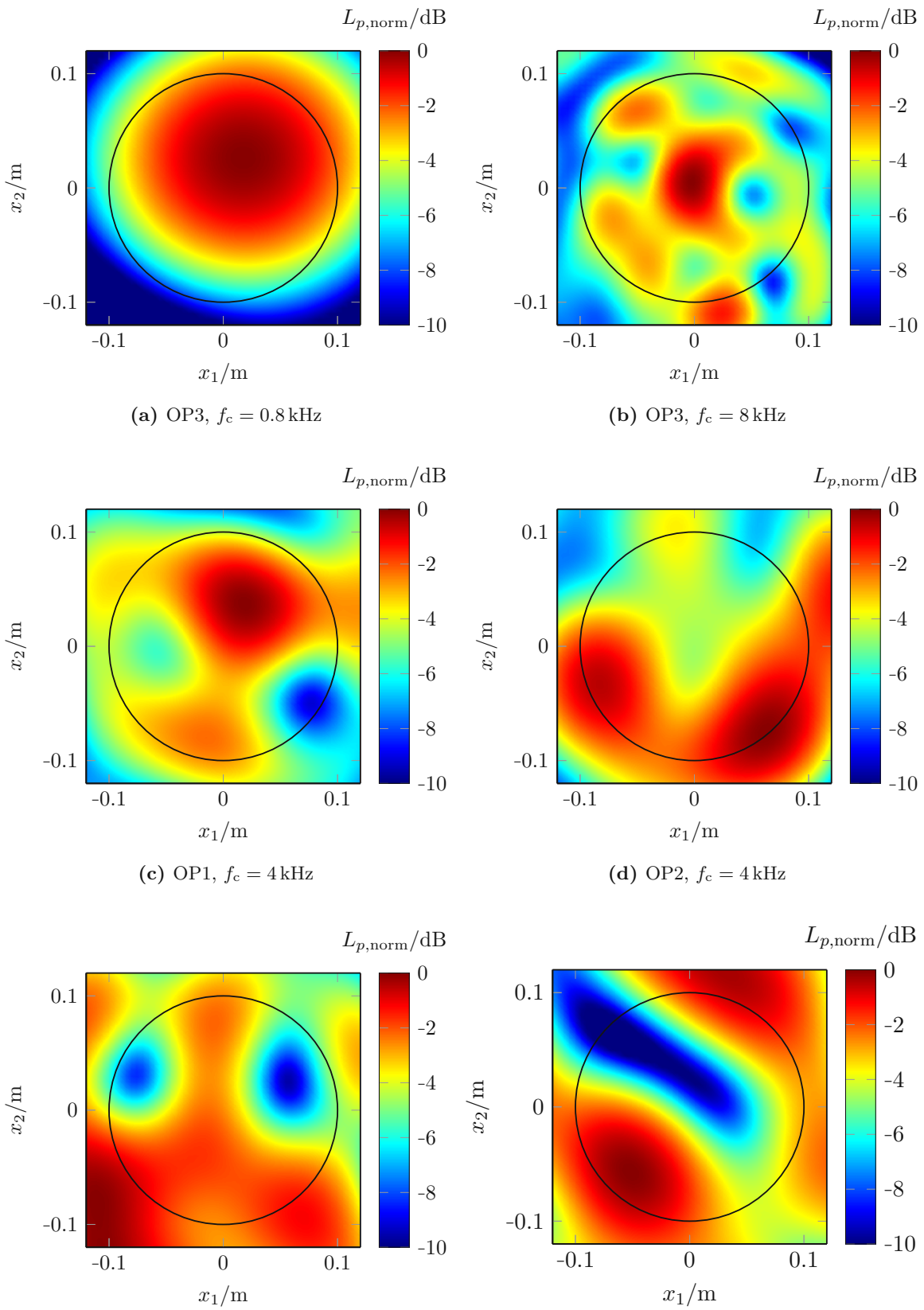

(a) OP3, $f_c = 0.8\,\mathrm{kHz}$

(b) OP3, $f_c = 8\,\mathrm{kHz}$

(c) OP1, $f_c = 4\,\mathrm{kHz}$

(d) OP2, $f_c = 4\,\mathrm{kHz}$

(e) OP3, $f_c = 4\,\mathrm{kHz}$

(f) OP4, $f_c = 4\,\mathrm{kHz}$

Fig. 4.11. Beamforming results of the performed microphone array measurements.

Chapter 5

Acoustic optimisation

5.1 Absorber design and placement

The absorber linings designed were laid out as single perforate absorbers with a partitioned backing cavity and MPPs as absorber material. Microperforated plates called *MASH* from the company *fteu* were provided by the Institute of Mechanics and Mechatronics of the Vienna University of Technology [60]. The facesheet material utilised for the subsequent absorber design was stainless steel. However, aluminium is also available as a material for the selected MPPs, which could be beneficial given further considerations about lightweight construction. As parameters of the facesheet, its perforation rate $\epsilon = 0.152$ and thickness $t = 0.7\,\mathrm{mm}$ are given.

Because the above-mentioned MPPs are not perforated with cylindrical holes, but rather complex slit-shaped pattern, as presented in Fig. 5.1a, the perforation diameter a for the calculation of the absorption coefficient was not provided directly. As it does not affect the absorption's frequency range, but only the absorption coefficient's maximum value it was assumed to be $a = 0.05\,\mathrm{mm}$, which yielded high-absorbing results at the absorption maxima

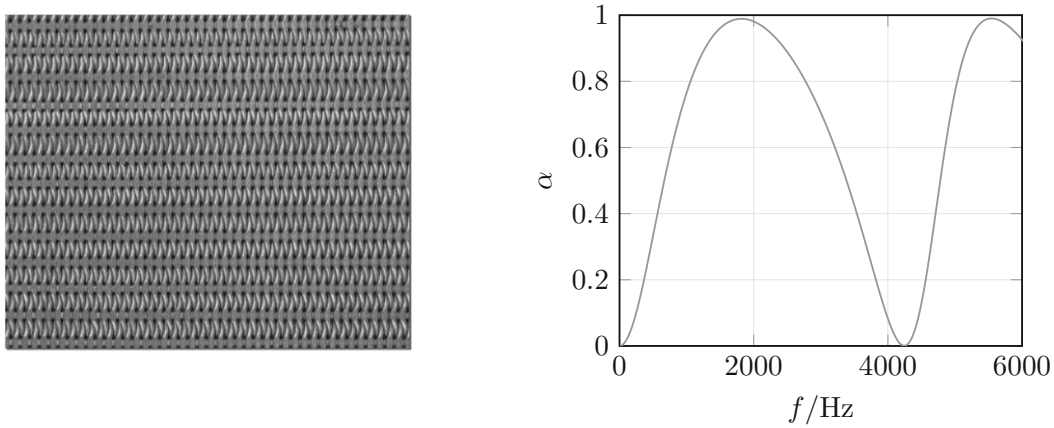

(a) *MASH* perforation pattern, from [60].

(b) Laid out absorption coefficient.

Fig. 5.1. Facesheet structure and computed absorption coefficient of designed absorber linings.

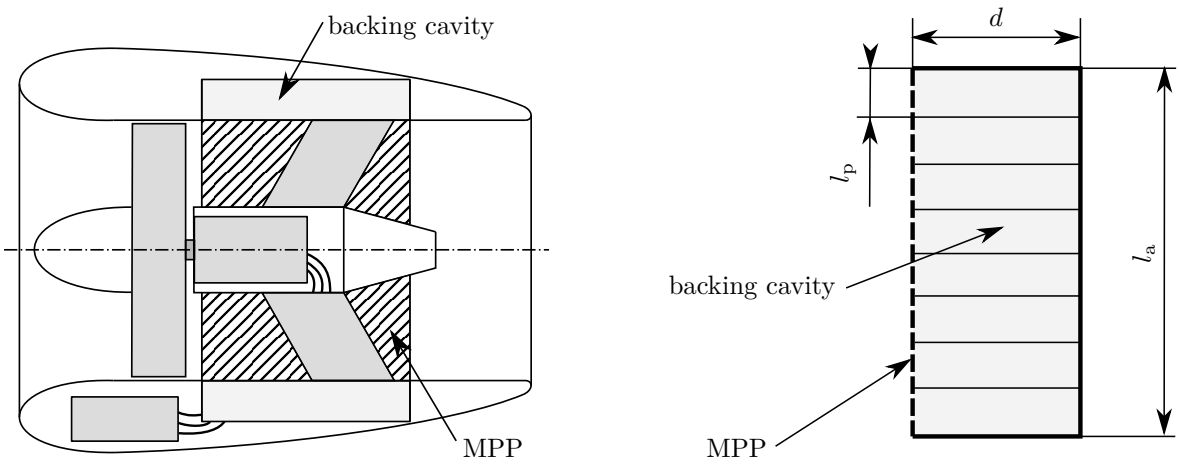

(a) Placement in EDF. **(b)** Design of MPA.

Fig. 5.2. Design and placement of absorber linings.

based on previous experience using this MPP material. Therefore, valid statements on the absorption coefficient's absolute value cannot be made. As a backing cavity depth of $d = 40\,\text{mm}$ was chosen, which already pushed the geometric limits of the fan unit's aerodynamic shell. In Fig. 5.2a, the limiting shell is indicated towards the exhaust pipe, as well as a limited extent towards the inlet lip due to the avoidance of absorbers in the rotor plane, which would reduce the fan's aerodynamic efficiency [51]. The designed absorber lining's resulting absorption coefficient for a normal incident plane wave was computed by a *MATLAB*-script from [61] and is shown in Fig. 5.1b for the preceding values. The absorption maximum in the lower frequency range at 1800 Hz is close to the fan unit's BPF at OP4, which represents the maximum tonal SPL for the examined operating range. The highest broadband SPL will also be partially absorbed by the absorber designed, as the second maximum of the absorption coefficient occurs at 5500 Hz.

The partitioning and placement of the absorber linings designed is presented in Fig. 5.2. As can be seen in Fig. 5.2b, the backing cavity of the absorber linings designed is partitioned to increase the absorption of random incident sound pressure waves. A cake piece partitioning resulted for the rectangular segment cross sections, which was dimensioned according to former research insights [48]. The absorber linings where placed in the stator vane section only around the EDF unit's duct, in order not to disturb the aerodynamics at the rotor tip section. This resulted in a relative absorption area of 16.6 % of the total inner duct area.

5.2 Measurement results

In order to examine the impact of the absorber linings designed on the fan unit's acoustic emissions, the measurements from Chap. 4.2 were retaken using the unchanged measuring setup and positioning of the modified measuring object. Additionally, measurements from the electric powertrain were taken without the rotor attached to examine its acoustic properties.

5.2.1 Far-field radiation

In Fig. 5.3a and Fig. 5.3b, the narrowband SPLs measured at the exhaust and inlet position, respectively are shown for the modified, as well as the unmodified fan unit. As expected, the change in the fan unit's acoustic emissions due to the modifications performed depends on the observer position. The SPL at the BPF and its harmonics are dampened more at the outlet position than on the inlet position. The higher absorption can be explained by considering the rotor self-noise's propagation path towards the microphones. As the absorber linings are positioned behind the rotor, the rotor self-noise has to pass the duct section containing the absorbers. For the inlet facing observer positions, a greater part of the acoustic pressure waves reach the observer unreflected and, therefore, unattenuated. Nevertheless, the SPL peaks that can be associated with the rotor-stator interaction are also attenuated before reaching the inlet microphone position. The broadband noise between 1400 Hz and 2000 Hz is significantly dampened at the outlet microphone position, which accounts for the correct layout of the absorber linings.

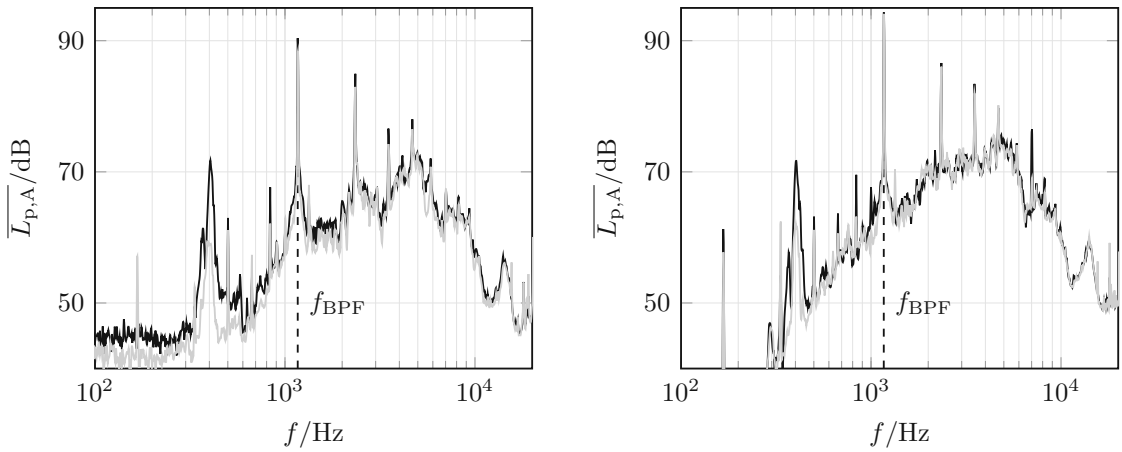

(a) Microphone position 5 **(b)** Microphone position 8

Fig. 5.3. Narrowband $\overline{L}_{\mathrm{p,A}}$ at microphone positions 5 and 8 of EDF at OP3 of unmodified (——) and modified (——) EDF unit.

The narrowband SPLs at 350 Hz and 400 Hz are by far the most attenuated frequency ranges at both microphone positions, as well as the low-frequency broadband sound between 100 Hz and 300 Hz at the outlet position. Given the circumstance, that the high absorption frequency range can technically not be as low due to the short backing cavity, the high attenuation of those low frequency SPL may evolve from influencing the respective source mechanisms by installing the MPAs to the fan unit.

In Fig. 5.4, the narrowband SPLs averaged over the enveloping surface are shown for the predefined operating points OP1 to OP4. The laid-out absorption frequency range can be made out by close examination of the BPF and its harmonics. At OP1 and OP2, only the SPL at the higher harmonics of the BPF are attenuated with the absorber modifications, while the SPL at the BPF is not attenuated. The SPL at the BPF is attenuated when entering the

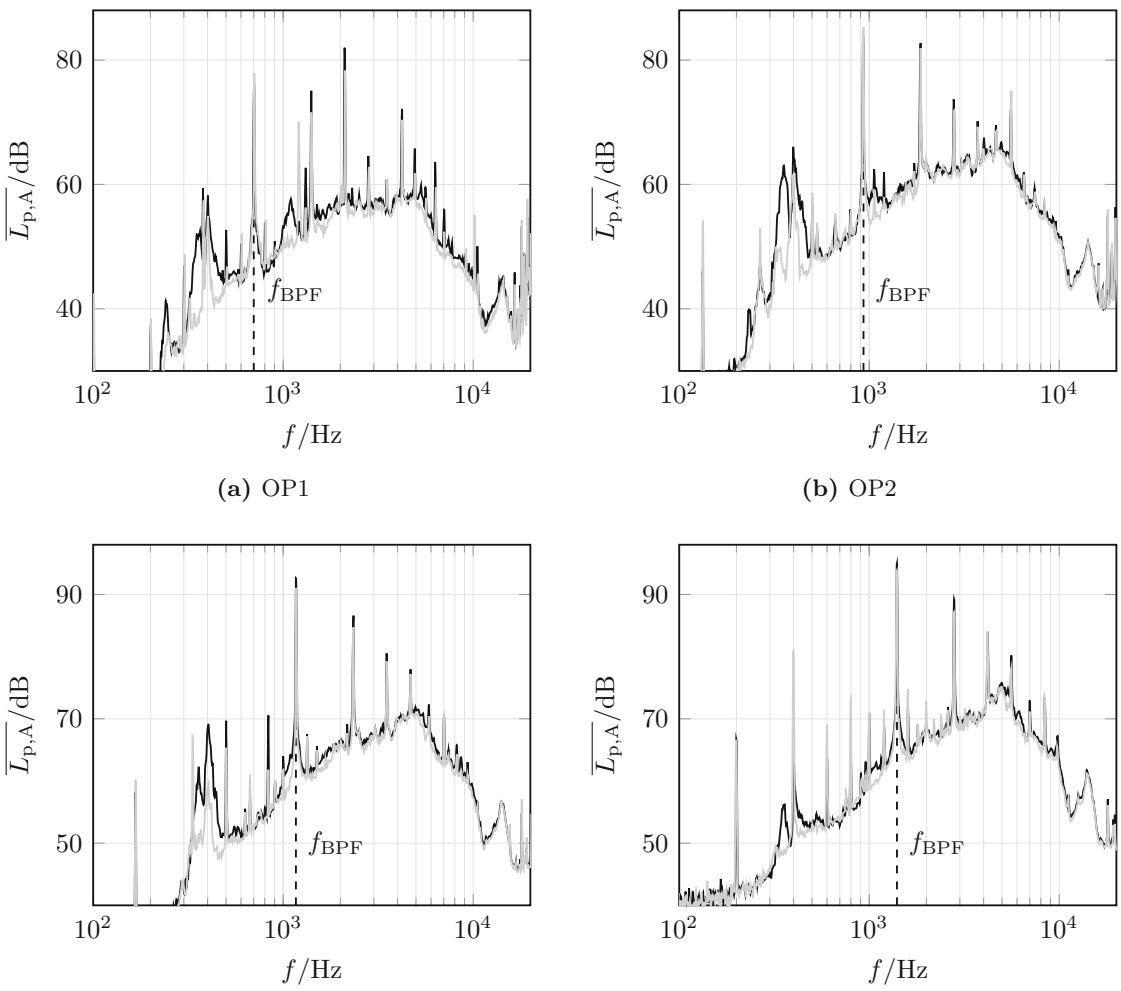

Fig. 5.4. Narrowband $\overline{L_{p,A}}$ at different operating points of unmodified (——) and modified (——) EDF unit.

high absorption frequency range of the absorber linings in OP3 and OP4. The attenuation effect on the narrowband SPL at 350 Hz and 400 Hz observed in Fig. 5.3 also occurs at the other operating points, which indicates its reproducibility. Nevertheless, amplification can also be seen - e.g. for the tonal frequencies below the BPF at OP4 and especially the SPL peak at 400 Hz.

In order to further discuss the acoustic characteristics of the modified EDF unit, transient measurements were conducted and postprocessed in the equal manner as for Fig. 4.9. In Fig. 5.5, the results for the spectrograms in the operating range of the modified EDF unit are presented. The spectrograms show the lower narrowband SPLs at 350 Hz and 400 Hz for the whole operating range. Moreover, the artefacts identified in Fig. 4.9 are notably lower in the measurement results from the modified fan unit compared to the unmodified fan unit. To form a statement on the change of the total sound emissions due to the absorber lining installation, the A-weighted OSPL was calculated for the frequency range considered and is compared with the OPL of the unmodified EDF unit in Fig. 5.6. Therewith, a consistent

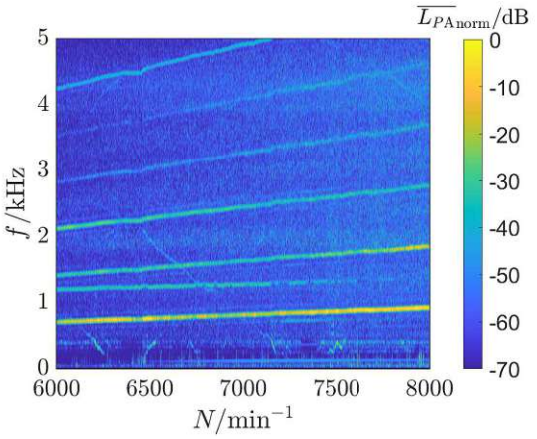

(a) Spectrogram between OP1 and OP2

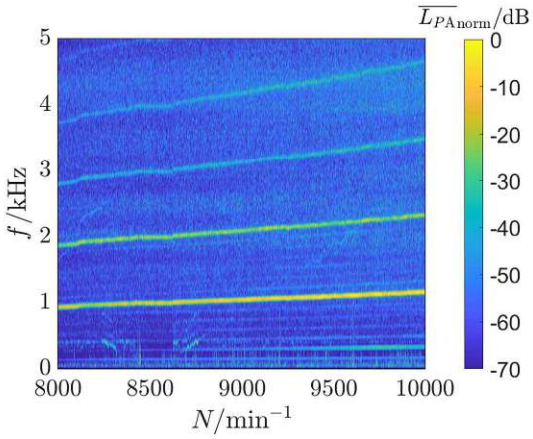

(b) Spectrogram between OP2 and OP3

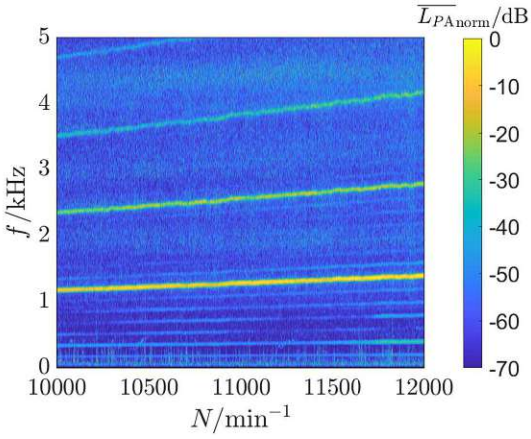

(c) Spectrogram between OP3 and OP4

Fig. 5.5. Spectrograms in the operating range of unmodified and modified EDF unit.

attenuation of the OSPL of more than 1 dB can be confirmed for the total operating range. The maximum attenuation between 9000 min^{-1} and 10 000 min^{-1} of as much as 4 dB can be also confirmed by close examination of Fig. 5.5b, where the SPL at the BPF no longer obtains a local maximum.

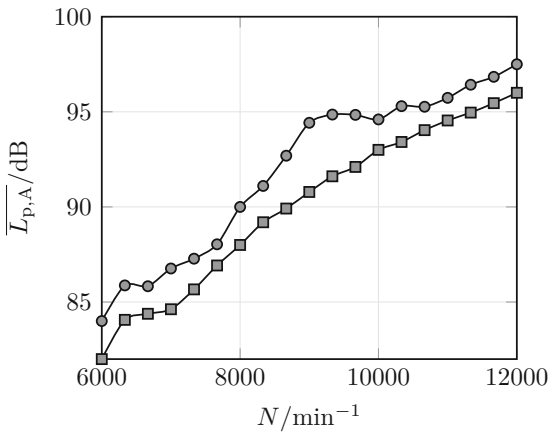

Fig. 5.6. A-weighted OSPL over operating range of unmodified (—●—) and modified (—■—) EDF unit.

5.2.2 Examination of the electric powertrain

The electric powertrain was measured acoustically solely without the aerodynamic rotor attached to the motor shaft and with the absorber linings installed. The ECM and inverter sound emissions' spectrum can be examined more closely with this setup. However, an evaluation of the SPL amplitudes cannot be made, as the motor currents and respective electromagnetic forces are significantly lower for the motor without load. In Fig. 5.7, the powertrain measurement results at the four operating points are shown. At OP1, the highest SPL measured without load occurs at 2100 Hz, which is the third harmonic of the BPF for the EDF system. The electric powertrain can be the main source mechanism for this tonal noise component owing to the fact that the SPL at this frequency also is the EDF's highest SPL at OP1. The overall spectra at all operating points obtain many tonal components at multiplicities of the rotational speed, which indicates electromagnetic local and global forces as sound mechanisms. In particular, the SPL at the first harmonic frequency of rotational speed is clearly present at all operating points and yields an explanation for the same behaviour in the EDF unit. The narrowband SPLs at 350 Hz and

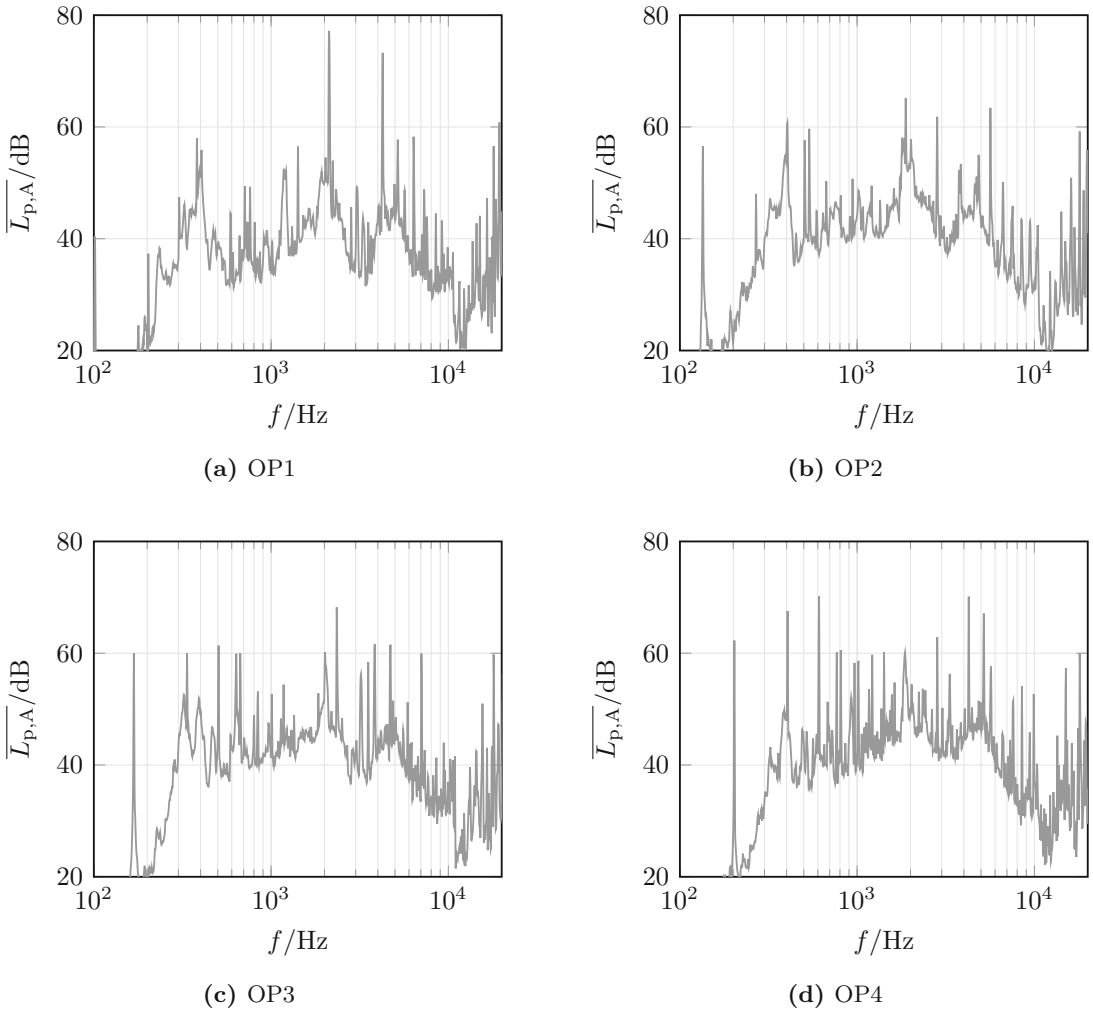

Fig. 5.7. Narrowband $\overline{L_{p,A}}$ at different operating points of unmodified and modified EDF unit.

400 Hz also appear in the measurements of the electric powertrain, which excludes the aerodynamic rotor as their noise source. As the frequencies of these narrowband SPLs are independent of the fan's rotational speed, a possible explanation might be acoustic resonances of the motor's internal airspace between rotor and stator, which has already been analysed for a different ECM model in [30]. However, this does not explain the high absorption accomplished for these frequency components by applying the absorber linings designed.

Spectrograms are plotted for the whole operating range in Fig. 5.8 for better visualization of the frequency component's dependency on rotational speed. The tonal frequency components at the main electromagnetic frequency f_{LF} and its harmonics are notably visible. The tonal noise emission at $f = \frac{3}{2} f_{\mathrm{LF}}$ in the lower and upper speed range of the considered operating range considered is also clearly dominant, which can result from cogging torque characteristics of the ECM. The artefact forms that first decrease their frequency with increasing rotational speed, are also seen in the measurement results from the electric powertrain. Accordingly, the respective source mechanism can be assigned to electronic components. One explanation can be a commutation operating principle of the inverter, but to prove this hypothesis a closer

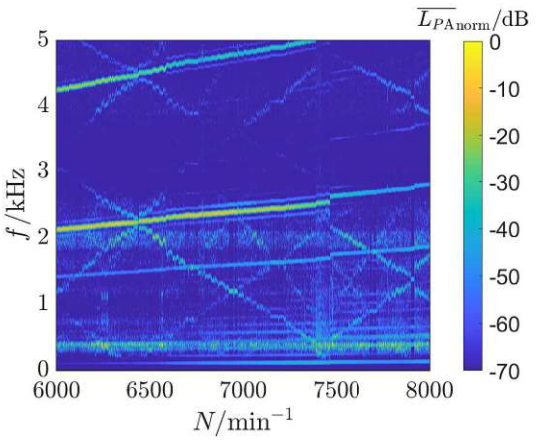

(a) Spectrogram between OP1 and OP2

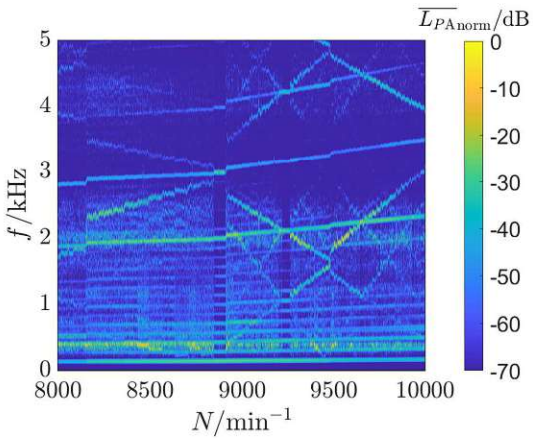

(b) Spectrogram between OP2 and OP3

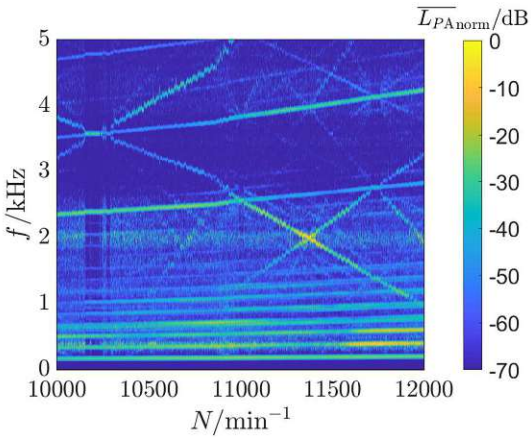

(c) Spectrogram between OP3 and OP4

Fig. 5.8. Spectrograms of the electric powertrain in the fan unit's operating range.

electric examination of the electronic components needs to be conducted.

Chapter 6

Summary and outlook

In the present thesis, experimental research was conducted on a subscale EDF unit, to characterize its acoustics and explore the possibilities of noise abatement through applying second measures. The axial fan unit was measured acoustically using the enveloping surface method and microphone array measurements. Enveloping surface method measurements were conducted for an essentially free field over a reflecting plane according to international standard DIN EN ISO 3744 to gain knowledge about the EDF unit's acoustic far-field emissions, while the microphone array measurements aimed at examining the acoustic source distribution of the rotor.

The findings concerning the EDF unit's far-field emissions, allocated the highest tonal SPL to the BPF and its harmonic frequencies, while the highest broadband noise sources were found to come from the rotor itself. Through acoustic measurements of the electric powertrain without the aerodynamic rotor attached also caused significant tonal noise emissions from the electric motor, which were identified to superimpose the higher harmonics of the BPF and the SPL of the noises resulting from rotor-stator interaction. By performing transient measurements across the entire operating range, spectrograms could be computed and consulted to prove characteristics for the wide regions of the operating range. Unexpected tonal artefacts with negative frequency proportionality to the rotational speed were noticed within this. These artefacts could also be proven by the powertrain measurements not to have their source mechanism lying in aerodynamics, but rather in the electronic components.

Given the findings made about the EDF's acoustic characteristics, perforate absorber linings were laid out to effectively absorb the sound pressure waves with the highest amplitude, which is represented by the BPF. After designing and manufacturing the absorber linings, the modified EDF was measured once again and a resulting reduction in the SPL was noticed. The A-weighted OSPL was reduced 2-4 dB across the total operating range of the EDF unit, whereas certain frequency sections were attenuated by up to 10 dB.

Outlook

Many partial aspects of EDF acoustics were dealt with only briefly due to the limited resources available for this thesis. Further refinement of the microphone array setup and configuration as remarked in Chap. 4.2.2 can provide a more exact localisation of acoustic broadband sources as well as enable the possibility of localising sources at different frequency bands. Another advanced possibility to measure the in-duct acoustics more precisely can be provided by in-duct microphone arrays [62].

The fan rotor can be measured while driven externally for further characterisation of the single EDF components. In order to gain more valid insights into the acoustic behaviour of the electric powertrain, it could be measured under a silent load. Furthermore, electric measurements and electromagnetic simulations of the ECM can be conducted to determine the electromagnetic force oscillations acting and conclude to the SPL emitted.

The absorber linings designed can be measured by the use of an impedance tube to estimate the actual absorption coefficient. Moreover, double DoF absorber designs and other facesheet materials can be examined to attenuation potential for the observed EDF. For more advanced absorber design, a simulation model of the EDF can be set up to evaluate the effects of possible absorber linings on propagation and radiation of the sound emissions to the far-field.

Bibliography

[1] Air Transport Action Group (ATAG), *Aviation/Benefits beyond Borders: Global Summary*. ATAG Geneva, Switzerland, 2018.

[2] International Civil Aviation Organization (ICAO), "Annual report 2018 - the world of air transport in 2018." `https://www.icao.int/annual-report-2018/Pages/the-world-of-air-transport-in-2018.aspx`, 2018. [Online; accessed October 19, 2020].

[3] D. L. Huff, "Nasa glenn's contributions to aircraft engine noise research," *Journal of Aerospace Engineering*, vol. 26, no. 2, pp. 218–250, 2013.

[4] M. J. Smith, *Aircraft noise*, vol. 3. Cambridge University Press, 2004.

[5] H. Ising and B. Kruppa, "Zum gegenwärtigen Erkenntnisstand der Lärmwirkungsforschung: Notwendigkeit eines Paradigmenwechsels," *Umweltmedizin in Forschung und Praxis*, vol. 6, no. 4, pp. 181–189, 2001.

[6] International Civil Aviation Organization (ICAO), "Environmental technical manual - volume i procedures for the noise certification of aircraft," in *1st Edition*, 2012.

[7] International Civil Aviation Organization (ICAO), "Environmental protection - volume i aircraft noise," in *5th Edition*, 2008.

[8] VOLARE GmbH, "Volare gmbh." `https://www.apeleon.com/index.php/de/home-de/`, 2020. [Online; accessed October 19, 2020].

[9] K. Pascioni and S. A. Rizzi, "Tonal noise prediction of a distributed propulsion unmanned aerial vehicle," in *2018 AIAA/CEAS Aeroacoustics Conference*, p. 2951, 2018.

[10] H. D. Kim, A. T. Perry, and P. J. Ansell, "A review of distributed electric propulsion concepts for air vehicle technology," in *2018 AIAA/IEEE Electric Aircraft Technologies Symposium (EATS)*, pp. 1–21, IEEE, 2018.

[11] R. Müller, *Luftstrahltriebwerke: Grundlagen, Charakteristiken Arbeitsverhalten*. Springer-Verlag, 2013.

[12] R. Royce, *The jet engine*. John Wiley & Sons, 2015.

[13] J. M. Tyler and T. G. Sofrin, "Axial flow compressor noise studies," tech. rep., SAE Technical Paper, 1962.

[14] F. J. Krömer, *Sound emission of low-pressure axial fans under distorted inflow conditions*. Doctoral thesis, FAU University Press, 2018.

[15] T. F. Brooks, D. S. Pope, and M. A. Marcolini, "Airfoil self-noise and prediction," *NASA Reference Publication 1218*, 1989.

[16] J. Griffiths, "The spectrum of compressor noise of a jet engine," *Journal of Sound and Vibration*, vol. 1, no. 2, pp. 127–140, 1964.

[17] J. Groeneweg and E. J. Rice, "Aircraft turbofan noise," *Journal of Turbomachinery*, vol. 109, pp. 131–141, 1987.

[18] C. Feiler and J. Groeneweg, "Summary of forward velocity effects on fan noise," in *4th Aeroacoustics Conference*, p. 1319, 1977.

[19] W. Neise and U. Michel, "Aerodynamic noise of turbomachines," *Deutsche Forschungsanstalt für Luft-und Raumfahrt, eV, DLR, Institut für Strömungsmechanik, Abt. Turbulenzforschung, Berlin*, vol. 5, 1994.

[20] E. Envia, A. G. Wilson, and D. L. Huff, "Fan noise: a challenge to caa," *International Journal of Computational Fluid Dynamics*, vol. 18, no. 6, pp. 471–480, 2004.

[21] F. Han, A. Sharma, U. Paliath, and C. Shieh, "Multiple pure tone noise prediction," *Journal of Sound and Vibration*, vol. 333, no. 25, pp. 6942–6959, 2014.

[22] M. Möser, *Messtechnik der Akustik*. Springer-Verlag, 2009.

[23] W. Copeland and J. Crigler, "Experimental noise studies of inlet-guide-vane-rotor-stator interactions for a single-stage axial-flow compressor," 1965.

[24] E. Envia and M. Nallasamy, "Design selection and analysis of a swept and leaned stator concept," 1998.

[25] R. P. Woodward, D. M. Elliott, C. E. Hughes, and J. J. Berton, "Benefits of swept-and-leaned stators for fan noise reduction," *Journal of Aircraft*, vol. 38, no. 6, pp. 1130–1138, 2001.

[26] E. Envia, "Fan noise reduction: an overview," *International Journal of Aeroacoustics*, vol. 1, no. 1, pp. 43–64, 2002.

[27] S. Kaji and T. Okazaki, "Generation of sound by rotor-stator interaction," *Journal of Sound and Vibration*, vol. 13, no. 3, pp. 281–307, 1970.

[28] M. J. Lighthill, "On sound generated aerodynamically ii. turbulence as a source of sound," *Proceedings of the Royal Society of London. Series A. Mathematical and Physical Sciences*, vol. 222, no. 1148, pp. 1–32, 1954.

[29] R. L. Balzer, "Segmented mixing device having chevrons for exhaust noise reduction in jet engines," Sept. 2 2003. US Patent 6,612,106.

[30] H. J. Lee, S. U. Chung, and S. M. Hwang, "Noise source identification of a bldc motor," *Journal of mechanical science and technology*, vol. 22, no. 4, p. 708, 2008.

[31] P. Yedamale, "Brushless dc (bldc) motor fundamentals," *Microchip Technology Inc*, vol. 20, pp. 3–15, 2003.

[32] H.-S. Ko and K.-J. Kim, "Characterization of noise and vibration sources in interior permanent-magnet brushless dc motors," *IEEE Transactions on Magnetics*, vol. 40, no. 6, pp. 3482–3489, 2004.

[33] E. Rice, "Spinning mode sound propagation in ducts with acoustic treatment and sheared flow," in *2nd Aeroacoustics Conference*, p. 519, 1975.

[34] S. W. Rienstra, "Fundamentals of duct acoustics," *Von Karman Institute Lecture Notes*, 2015.

[35] S. Lewy, "Inverse method predicting spinning modes radiated by a ducted fan from free-field measurements," *The Journal of the Acoustical Society of America*, vol. 117, no. 2, pp. 744–750, 2005.

[36] X. Zhang, X. Chen, C. Morfey, and P. Nelson, "Computation of spinning modal radiation from an unflanged duct," *AIAA journal*, vol. 42, no. 9, pp. 1795–1801, 2004.

[37] M. De Marchis, E. Napoli, and V. Armenio, "Turbulence structures over irregular rough surfaces," *Journal of Turbulence*, no. 11, p. N3, 2010.

[38] X. Yu, L. Cheng, Y. Tong, and J. Pan, "Sound attenuation using duct silencers with micro-perforated panel absorbers," in *INTER-NOISE and NOISE-CON Congress and Conference Proceedings*, vol. 249, pp. 752–759, Institute of Noise Control Engineering, 2014.

[39] X. Yu and L. Cheng, "Duct noise attenuation using reactive silencer with various internal configurations," *Journal of sound and vibration*, vol. 335, pp. 229–244, 2015.

[40] G. J. Ruijgrok, *Elements of aviation acoustics.* Delft University Press, 1993.

[41] T. J. Cox and P. D'antonio, *Acoustic absorbers and diffusers: theory, design and application.* Crc Press, 2017.

[42] J. Metzger, *Characterization of Acoustic Absorbers.* Vienna University of Technology, 2017.

[43] M. Kaltenbacher, *Skriptum zur Vorlesung Strömungsakustik.* Vienna University of Technology, 2019.

[44] M. Dannemann, M. Kucher, E. Kunze, N. Modler, K. Knobloch, L. Enghardt, E. Sarradj, and K. Höschler, "Experimental study of advanced helmholtz resonator liners with

increased acoustic performance by utilising material damping effects," *Applied Sciences*, vol. 8, no. 10, p. 1923, 2018.

[45] U. Ingard, "On the theory and design of acoustic resonators," *The Journal of the acoustical society of America*, vol. 25, no. 6, pp. 1037–1061, 1953.

[46] D.-Y. Maa, "Potential of microperforated panel absorber," *the Journal of the Acoustical Society of America*, vol. 104, no. 5, pp. 2861–2866, 1998.

[47] I. L. Ver and L. L. Beranek, *Noise and Vibration Control Engineering-Principles and Applications, Wiley, 2006: Noise and Vibration Control Engineering-Principles and Applications*, vol. 1. Bukupedia, 2006.

[48] J. Liu and D. Herrin, "Enhancing micro-perforated panel attenuation by partitioning the adjoining cavity," *Applied Acoustics*, vol. 71, no. 2, pp. 120–127, 2010.

[49] H. V. Fuchs and X. Zha, "Micro-perforated structures as sound absorbers–a review and outlook," *Acta acustica united with acustica*, vol. 92, no. 1, pp. 139–146, 2006.

[50] D. Geng, K. Yi, C. Shang, J. Yang, and Y. He, "Application status of composite acoustic liner in aero-engine," in *Proceedings of the 10th International Conference on Composite Science and Technology, Lisboa, Portugal*, pp. 2–4, 2015.

[51] S. Floss, F. Czwielong, F. Krömer, S. Becker, and M. Kaltenbacher, "Achieving axial fan sound reduction with micro-perforated absorbers," *Vienna University of Technology*, 2019.

[52] SONATECH GmbH + Co. KG, "Baso plan - absorber material." `https://www.sonatech.de/privat/decke/weichschaumstoff/baso-plan.html?language=d`, 2020. [Online; accessed October 19, 2020].

[53] D. e.V., *3744: 2011-02: Akustik – Bestimmung der Schallleistungs- und Schallenergiepegel von Geräuschquellen aus Schalldruckmessungen – Hüllflächenverfahren der Genauigkeitsklasse 2 für ein im Wesentlichen freies Schallfeld über einer reflektierenden Ebene (ISO 3744: 2010)*. Beuth-Verlag, Berlin, 2011.

[54] D. e.V., *3745: 2012-07: Akustik – Bestimmung der Schallleistungs- und Schallenergiepegel von Geräuschquellen aus Schalldruckmessungen – Hüllflächenverfahren der Genauigkeitsklasse 1 für reflexionsarme Räume und Halbräume (ISO 3745: 2012 + Amd 1:2017)*. Beuth-Verlag, Berlin, 2012.

[55] ISO/IEC, *IS 26101: 2017-04: Acoustics — Test methods for the qualification of free-field environments*. International Organization for Standardization, Geneva, Switzerland, 2017.

[56] M. W. WOLFGANG, *Formeln und Tabellen Bauphysik: Wärmeschutz – Feuchteschutz – Klima – Akustik – Brandschutz*. MORGAN KAUFMANN, 2018.

[57] D. e.V., *3382-2: 2008-09: Messung von Parametern der Raumakustik – Teil 2: Nachhallzeit in gewöhnlichen Räumen (ISO 3382-2:2008)*. Beuth-Verlag, Berlin, 2008.

[58] J. Nowak, *Schallquellenortung an rotierenden Systemen*. Vienna University of Technology, 2018.

[59] R. P. Dougherty, R. C. Ramachandran, and G. Raman, "Deconvolution of sources in aeroacoustic images from phased microphone arrays using linear programming," *International Journal of Aeroacoustics*, vol. 12, no. 7-8, pp. 699–717, 2013.

[60] fteu, "Mash - fibre-free sound absorption." `https://https://fteu.eu/technology/mash/`, 2020. [Online; accessed October 19, 2020].

[61] L. Jaouen and F.-X. Bécot, "Acoustical characterization of perforated facings," *The Journal of the Acoustical Society of America*, vol. 129, no. 3, pp. 1400–1406, 2011.

[62] C. Lowis, P. Joseph, and A. Kempton, "Estimation of the far-field directivity of broadband aeroengine fan noise using an in-duct axial microphone array," *Journal of Sound and Vibration*, vol. 329, no. 19, pp. 3940–3957, 2010.